
Periodic Activation Functions Induce Stationarity

Lassi Meronen
Aalto University / Saab Finland Oy
Espoo, Finland
lassi.meronen@aalto.fi

Martin Trapp
Aalto University
Espoo, Finland
martin.trapp@aalto.fi

Arno Solin
Aalto University
Espoo, Finland
arno.solin@aalto.fi

Abstract

Neural network models are known to reinforce hidden data biases, making them unreliable and difficult to interpret. We seek to build models that ‘know what they do not know’ by introducing inductive biases in the function space. We show that *periodic* activation functions in Bayesian neural networks establish a connection between the prior on the network weights and translation-invariant, stationary Gaussian process priors. Furthermore, we show that this link goes beyond sinusoidal (Fourier) activations by also covering triangular wave and periodic ReLU activation functions. In a series of experiments, we show that periodic activation functions obtain comparable performance for in-domain data and capture sensitivity to perturbed inputs in deep neural networks for out-of-domain detection.

1 Introduction

Deep feedforward neural networks [46, 16] are an integral part of contemporary artificial intelligence and machine learning systems for visual and auditory perception, medicine, and general data analysis and decision making. However, when these methods have been adopted into real-world use, concerns related to robustness (with respect to data that has not been seen during training), fairness (hidden biases in data being reinforced by the model), and interpretability (why the model acts as it does) have taken a central role. The knowledge gathered by contemporary neural networks has even been characterised as never truly reliable [31]. These issues relate to the sensitivity of the trained model to perturbed inputs being fed through it—or the lack thereof.

This motivates *Bayesian deep learning*, where the interests are two-fold: encoding prior knowledge into models and performing probabilistic inference under the specified model. We focus on the former. Probabilistic approaches to specifying assumptions about the function space of deep neural networks have gained increasing attention in the machine learning community, comprising, among others, work analysing their posterior distribution [57, 1], discussing pathologies arising in uncertainty quantification [9], and calls for better Bayesian priors (*e.g.*, [42, 50, 37, 10]).

In this paper, we focus on stationary models, which act as a proxy for capturing *sensitivity*. Stationarity indicates translation-invariance, meaning that the joint probability distribution does not change when the inputs are shifted. This seemingly naive assumption has strong consequences in the sense that it induces *conservative* behaviour across the input domain, both in-distribution and outside the observed data. The resulting model is mean-reverting outside the training data (reversion to the prior), directly leading to higher uncertainty for out-of-distribution (OOD) samples (see Fig. 1 for examples). These features (together with some direct computational benefits) have made stationary models/priors the standard approach in kernel methods [4, 20], spatial statistics [5], and Gaussian process (GP) models [44], where the kernel is often chosen to induce stationarity.

Neural networks are parametric models, which typically fall into the class of non-stationary models. Non-stationarity increases *flexibility* and is often a sought-after property—especially if the interest is solely in optimizing for accuracy on in-domain test data. In fact, all standard neural network

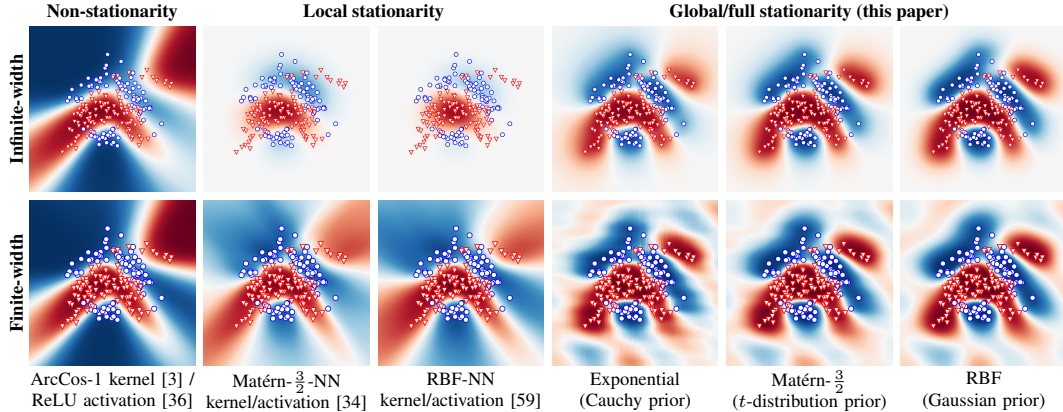


Figure 1: Posterior predictive densities of single hidden layer Bayesian neural networks (BNNs) with 30 hidden units and their infinite-width corresponding GPs on the banana classification task. Different activation functions induce different prior assumptions. Estimates obtained through HMC sampling [14] for 10k iterations.

activation functions (ReLU, sigmoid, *etc.*) induce non-stationarity (see [3, 59]). However, non-stationary models can easily result in over-confidence outside the observed data [18], [55] or spurious relationships between input variables (as illustrated in Fig. 1, where darker shades show higher confidence).

Stationarity in neural networks has been tackled before under the restriction of local stationarity, *i.e.*, translation-invariance is only *local*, induced by a Gaussian envelope (as realized by [59] for the RBF kernel/activation). Recently, Meronen et al. [34] expanded this approach and derived activation functions corresponding to the widely used Matérn class of kernels [32, 44]. We go one step further and derive activation functions that induce *global* stationarity. To do so, we leverage theory from harmonic analysis [58] of periodic functions, which helps expand the effective support over the entire input domain. We also realize direct links to previous works leveraging harmonic functions in neural networks [13, 2, 61, 47, 56], and Fourier features in other model families [43, 51].

The contributions of this paper are: (i) We show that periodic activation functions establish a direct correspondence between the prior on the network weights and the spectral density of the covariance function of the limiting stationary Gaussian process (GP) of single hidden layer Bayesian neural networks (BNNs). (ii) We leverage this correspondence and show that placing a Student- t prior on the weights of the hidden layer corresponds to a prior on the function space with Matérn covariance. (iii) Finally, we show in a range of experiments that periodic activation functions obtain comparable performance for in-domain data, do not result in overconfident predictions, and enable robust out-of-domain detection.

1.1 Related Work

We build upon prior work on exploring the covariance function induced by different activation functions, starting with the seminal work by Williams [59], who discussed a sigmoidal (ERF) and a Gaussian (RBF) activation function, resulting in a locally stationary kernel modulated by a Gaussian envelope. Cho and Saul [3] introduced non-stationary GP kernels corresponding to the ReLU and step activations, and [54] later extended the approach to the leaky ReLU and analysed alternative weight prior specifications. More recently, [34] derived activation functions corresponding to kernels from the Matérn family, which are locally stationary modulated by Gaussian envelope. In addition to the work connecting neural networks to GPs at initialisation, [21] created a connection between the neural network training and kernel methods by introducing the Neural Tangent Kernel (NTK).

At the same time, uninformative priors have been widely criticised in Bayesian deep learning [10], and alternative strategies have been proposed to incorporate prior knowledge. Pearce et al. [42] proposed compositions of BNNs to mimic compositional kernels in their limiting case. Sun et al. [50] proposed a variational objective for BNNs acting on the function space rather than the network parameters. Nalisnick et al. [37] proposed tractable priors on the functional complexity, obtained through the change of variables formula applied to the KL-divergence from a reference model/prior.

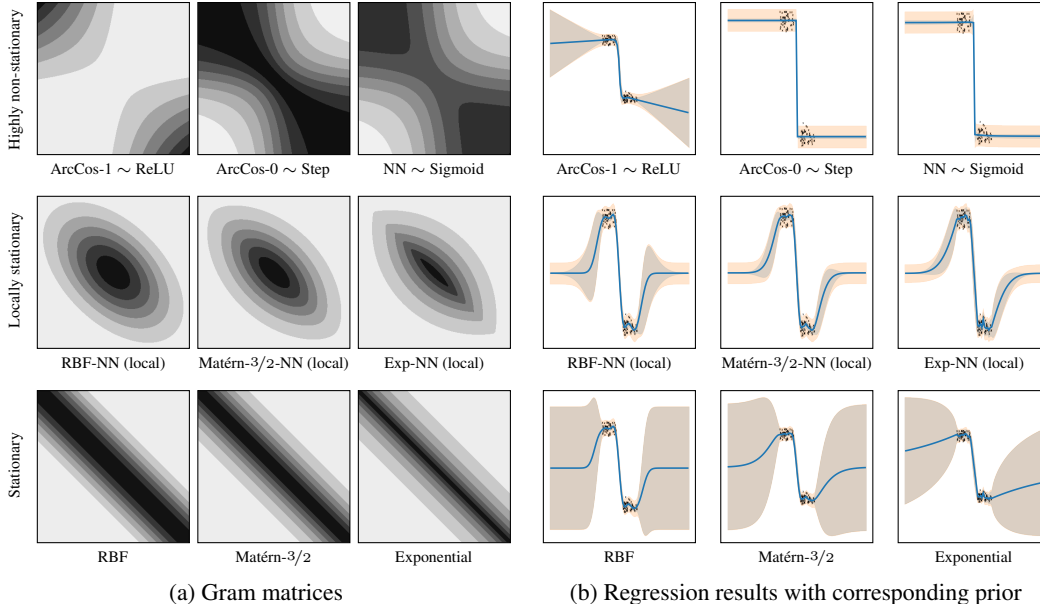


Figure 2: **Left:** Gram/covariance matrices (for $\kappa(x, x')$) reflecting different prior beliefs on how infinite-width NN model functions ought to behave outside the observed data. **Right:** 1D regression results corresponding to the model induced by the priors, showing the posterior \blacksquare and predictive 95% intervals. See Fig. 8 in appendix for the corresponding finite-width results.

Furthermore, Morales-Alvarez et al. [35] proposed to encode prior assumptions on the activation level rather than the model parameters.

Recent works have shown the potential of periodic activation functions in neural networks, including approaches to learn implicit neural representations [47], methods for recognition of handwritten digits [61], and out-of-distribution detection [30]. Earlier work used periodic activation functions to resemble the Fourier series [13, 56] and showed that such models are universal function approximators [2]. In broader terms, [27] recently showed that the use of the Fourier transform, replacing self-attention, in Transformers can drastically improve the runtime. Inspired by the Fourier duality of covariance and spectral density, [43] proposed random Fourier features to approximate a GP with an RBF kernel using Monte Carlo integration. [51] later analysed the quality of the approximation, and various works have explored (random or deterministic) Fourier features, *e.g.*, in the context of kernel methods (*e.g.*, [24, 19, 48]). [53] investigated the use of Fourier features in multilayer perceptrons (MLPs) to help represent high-frequency functions.

To the best of our knowledge, none of the previous works has shown that periodic activation functions in BNNs establish a direct correspondence between the prior on the network weights and the density of the spectral density decomposition, thus, inducing global stationarity and enabling principled prior choices for BNNs.

2 Encoding Inductive Biases into Infinitely-wide Networks

We are concerned with the notions of *similarity* and *bias* in the input space when performing supervised learning. For this, we consider modelling assumptions present in random (untrained) models that induce the *a priori* (before observing data) characteristics in the model. We argue that these assumptions, when combined with data, either reinforce or suppress data biases depending on the prior assumptions. For analysis, we consider the mean function, $\mu(\cdot)$, and covariance (kernel) function, $\kappa(\cdot, \cdot)$, induced by model functions $f(\mathbf{x})$, representing the input–output mapping of a single-layer: $\mu(\mathbf{x}) := \mathbb{E}[f(\mathbf{x})]$ and $\kappa(\mathbf{x}, \mathbf{x}') := \mathbb{E}[(f(\mathbf{x}) - \mu(\mathbf{x}))(f(\mathbf{x}') - \mu(\mathbf{x}'))^*]$, where $\mathbf{x}, \mathbf{x}' \in \mathbb{R}^d$ are two inputs and the expectations are taken over model functions. In probabilistic machine learning, rather than inferring the covariance structure from the expectations over model functions, one typically directly encodes assumptions by choosing a suitable parametric kernel family. However, both approaches, building a model by choosing a form for f or choosing a kernel family, are equivalent.

Specification of prior knowledge through the covariance function and doing inference under this model, is at the core of Gaussian process (GP) models [44]. These models admit the form of a prior $f(\mathbf{x}) \sim \mathcal{GP}(\mu(\mathbf{x}), \kappa(\mathbf{x}, \mathbf{x}'))$ and a likelihood (observation) model $\mathbf{y} | \mathbf{f} \sim \prod_{i=1}^n p(y_i | f(\mathbf{x}_i))$, where the data $\mathcal{D} = \{(\mathbf{x}_i, y_i)\}_{i=1}^n$ are input–output pairs and $\mathbf{x}_i \in \mathbb{R}^d$. This non-parametric machine learning paradigm covers regression and classification tasks, under which GPs are known to offer a convenient machinery for learning and inference, while offering meaningful uncertainty estimates.

Neal [38] showed that an untrained single-layer network converges to a GP in the limit of infinite width. This link is well-understood and generalizes to deep models [7], [26]. By placing an i.i.d. Gaussian prior on the weights and biases of a network, the distribution on the output of an untrained network converges to a Gaussian distribution in the limit of infinite width. By application of the multivariate Central Limit Theorem, the joint distribution of outputs for any collection of inputs is multivariate Gaussian, as in a GP, and completely characterized by some kernel function $\kappa(\cdot, \cdot)$. Let $\sigma(\cdot)$ be some non-linear (activation) function, such as the ReLU or sigmoid, and \mathbf{w} and b be the network weights and biases. Then, the associated kernel for the infinite-width network can be formulated in terms of [38, 12]:

$$\kappa(\mathbf{x}, \mathbf{x}') = \int p(\mathbf{w}) p(b) \sigma(\mathbf{w}^\top \mathbf{x} + b) \sigma(\mathbf{w}^\top \mathbf{x}' + b) d\mathbf{w} db, \quad (1)$$

where priors $p(\mathbf{w})$ and $p(b)$ are chosen suitably. From the formulation in Eq. (1) one can read that the covariance function corresponding to an untrained (random) single-layer neural network is *fully characterized* by the choice of activation function $\sigma(\cdot)$ and the priors on the network weights and biases.

Many of the covariance functions corresponding to commonly used activation functions under Gaussian priors on the weights have closed-form representations. The ArcCos kernel [3] covers the ReLU (ArcCos-1) and the step (ArcCos-0) activations, the so-called ‘neural network kernel’ [59, 44] links to sigmoidal activations. Gram matrices $\mathbf{K}_{ij} = \kappa(x_i, x'_j)$, evaluated for input pairs x and x' over $x, x' \in [-3, 3]$, are visualized in Fig. 2a to illustrate these covariance structures. The models induced by the ReLU, step, and sigmoid activations are by nature local, with the concentration of the non-linearity around the origin. As can be seen in the 1D regression results in Fig. 2b, the strong inductive bias in the prior (model) is reflected in the posterior. The ReLU extrapolates by matching the local bias of the data, while the step and sigmoidal saturate outside the data, and priors are clearly sensitive to translations and *highly non-stationary*.

Stationarity For a *stationary* (homogeneous) covariance function the covariance structure of the model functions $f(\mathbf{x})$ is the same regardless of the absolute position in the input space, and thus the parametrization can be relaxed to $\kappa(\mathbf{x}, \mathbf{x}') \triangleq \kappa(\mathbf{x} - \mathbf{x}') = \kappa(\mathbf{r})$. Stationarity implies translation-invariance, *i.e.* the notion of similarity between inputs \mathbf{x} , and \mathbf{x}' is only a function of their distance $\mathbf{x} - \mathbf{x}'$. This implies *weak stationarity* under stochastic process theory [40], and results in *reversion to the prior* outside observed data (see Fig. 2b). For stationary covariance functions, the best-known family is the Matérn [32, 49] family of kernels, which features models with sample functions of varying degrees of differentiability (smoothness):

$$\kappa_{\text{Mat.}}(\mathbf{x}, \mathbf{x}') = \frac{2^{1-\nu}}{\Gamma(\nu)} \left(\sqrt{2\nu} \frac{\|\mathbf{x} - \mathbf{x}'\|}{\ell} \right)^\nu K_\nu \left(\sqrt{2\nu} \frac{\|\mathbf{x} - \mathbf{x}'\|}{\ell} \right), \quad (2)$$

where ν is a smoothness parameter, ℓ a characteristic length-scale parameter, $K_\nu(\cdot)$ the modified Bessel function, and $\Gamma(\cdot)$ the gamma function. For the Matérn class, the processes are $\lceil \nu \rceil - 1$ times mean-square differentiable, and the family includes the RBF (squared exponential) and the exponential (Ornstein–Uhlenbeck) kernels as limiting cases as $\nu \rightarrow \infty$ and $\nu = 1/2$.

Local stationarity Neural networks do not naturally exhibit stationarity. Formally, this stems from the problem of representing non-linearities over an infinite input domain with a finite set of local non-linear mappings. However, to bridge the gap between neural networks and widely-used stationary kernels, the typical approach is to restrict the invariance to be *local* (see Fig. 2a). This is the approach in the RBF-NN [60, 44] and general Matérn-NN [34] activation functions, where the prior is a composite covariance function with a Gaussian decay envelope (see discussion in [15]), *i.e.*,

$$\kappa_{\text{Mat-NN}}(\mathbf{x}, \mathbf{x}') \propto \exp(-\mathbf{x}^\top \mathbf{x} / 2\sigma_m^2) \kappa_{\text{Mat.}}(\mathbf{x}, \mathbf{x}') \exp(-\mathbf{x}'^\top \mathbf{x}' / 2\sigma_m^2), \quad (3)$$

where $\sigma_m^2 = 2\sigma_b^2 + \ell^2$ (see Fig. 2a for the decay effect of the envelope). One motivation for this approach is to assume a Gaussian input density on the training/testing inputs, thus restricting our

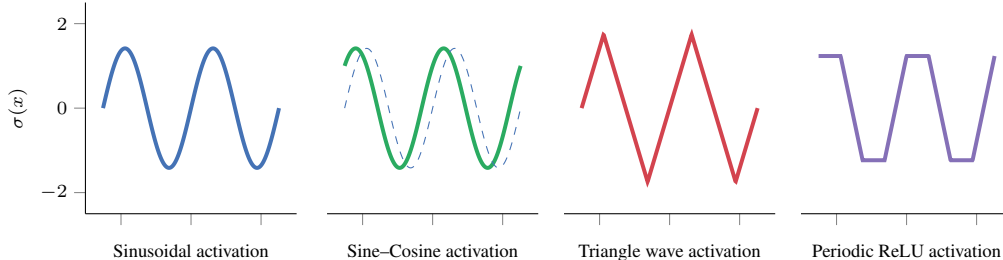


Figure 3: Sketches of types of periodic activations functions $\sigma(\cdot)$ visualized over two repeating periods each. The two leftmost are infinitely differentiable and the two rightmost are piecewise linear. The dashed line overlays the Sinusoidal activation for comparison.

interest only to inputs in the vicinity of the training data. The local behaviour is highlighted in Fig. 2b, where the locally stationary models revert to the mean (as expected), but the marginal uncertainty of the model functions drops to zero when far enough from training samples. This motivates us to seek activation functions that induce (globally) stationary behaviour (bottom-rows in Fig. 2).

3 Global Stationarity-inducing Activation Functions

We derive a direct connection between (fully) stationary covariance functions and periodic activation functions. Our main result leverages the spectral duality of the spectral density of stationary covariance functions to establish a direct connection between the weight prior and the induced prior on the function space. Furthermore, we show that this connection is not restricted to the (sinusoidal) Fourier basis and establishes an equivalence relationship between a Student- t distribution on the weights and a prior on the function space with Matérn covariance structure.

3.1 Spectral Duality Under Harmonic Functions

For stationarity-inducing priors, the covariance function can be written equivalently in terms of its spectral density function. This stems from *Bochner's theorem* (see [6] and 36A in [28] for a more general formulation) which states a bounded continuous positive definite function $\kappa(\mathbf{r})$ can be represented through the following norm-preserving isomorphism

$$\kappa(\mathbf{r}) = \int \omega(\mathbf{r}) \mu(d\omega), \quad (4)$$

where μ is a positive measure and $\mathbf{r} \in \mathbb{R}^d$. If the measure $\mu(\omega)$ has a density, it is called the *spectral density* $S(\omega)$ corresponding to the covariance function $\kappa(\mathbf{r})$. With $\omega(\mathbf{r}) = (2\pi)^{-d} \exp(i\omega^T \mathbf{r})$, this gives rise to the Fourier duality of covariance and spectral density, which is known as the *Wiener-Khinchin theorem* (e.g., [44]):

$$\kappa(\mathbf{r}) = \frac{1}{(2\pi)^d} \int S(\omega) e^{i\omega^T \mathbf{r}} d\omega \quad \text{and} \quad S(\omega) = \int \kappa(\mathbf{r}) e^{-i\omega^T \mathbf{r}} d\mathbf{r}. \quad (5)$$

For $d > 1$, if the covariance function is *isotropic* (it only depends on the Euclidean norm $\|\mathbf{r}\|$ such that $\kappa(r) \triangleq \kappa(\|\mathbf{r}\|)$), then it is invariant to all rigid motions of the input space. Moreover, the spectral density will also only depend on the norm of the dual input variable ω . In the neural network case, we can assume the previous layer will take care of scaling the inputs, and thus we effectively are interested in the isotropic case, which brings us to analysing 1D projections.

An important question is whether we are restricted to the (sinusoidal) Fourier basis. Let $\psi_j(x)$ be any sequence of bounded, square-integrable (over its period) periodic functions, such that these functions define an inner product space (generalising a basis of a vector space). In signal processing terms, they define a *frame* that provides a redundant yet stable way of representing a signal. From a generalised harmonic perspective [58], we could resort to any convenient basis, such as Gabor wavelets [11]. However, in this work we seek to choose $\psi(x)$ suitably, such that we have uniform convergence to $\omega(r)$ (cf., Eq. (4)), ensuring that we retain the spectral density $S(\omega)$.

3.2 Types of Periodic Activation Functions

We show how various periodic activation functions (see Fig. 4) under the view of Eq. (1) directly link back to the spectral duality. These periodic activation functions are continuous, bounded, and centered at zero, while not necessarily differentiable and never monotonic over \mathbb{R} (but monotonic within half-period).

Sinusoidal activation By assuming the activation function to be a sinusoid, $\sigma_{\sin}(x) = \sqrt{2} \sin(x)$ (see Fig. 4), placing a uniform prior on the bias term, $p(b) = \text{Uniform}(-\pi, \pi)$, and substituting this into Eq. (1), we can obtain an expression for the covariance function $\kappa(x, x')$:

$$\kappa(x, x') = \int p(w) \int_{-\pi}^{\pi} \frac{1}{\pi} \sin(wx + b) \sin(wx' + b) db dw. \quad (6)$$

By solving the inner integral and applying Euler’s formula ($\cos(z) = \frac{1}{2}(e^{iz} + e^{-iz})$), we obtain:

$$\kappa(x, x') = \frac{1}{2} \int p(w) e^{iw(x-x')} dw + \frac{1}{2} \int p(w) e^{-iw(x-x')} dw, \quad (7)$$

which simplifies under the assumption that the prior on the weight is symmetric and has support on the real line, *i.e.*,

$$\kappa(x, x') = \int p(w) e^{iw(x-x')} dw. \quad (8)$$

By letting $r = x - x'$, we find that we recover the spectral density decomposition of a stationary process given by the Wiener–Khinchin theorem in Eq. (5), where $p(w) = \frac{1}{2\pi} S(w)$. Therefore, we obtain a direct connection between the prior on the weights and the spectral density. A detailed derivation can be found in App. A.1.

Sine–Cosine activation An alternative way of using sinusoidal activation functions is the use of a composite sine–cosine activation, *i.e.*, $\sigma_{\sin \cos}(x) = \sin(x) + \cos(x)$ (Fig. 4 compares the sin–cos to the sinusoidal activation). Using such construction has the benefit of removing the need to integrate over the bias, which can result in reduced variance [51] of the estimates, giving us a covariance function in the form of:

$$\begin{aligned} \kappa(x, x') &= \int p(w) [\sin(wx) + \cos(wx)] [\sin(wx') + \cos(wx')] dw \\ &= \int p(w) \sin(w(x+x')) dw + \int p(w) \cos(w(x-x')) dw. \end{aligned} \quad (9)$$

By application of Euler’s formula and under the usual assumption that $p(w)$ is symmetric and has support on the entire real line, the above reduces to:

$$\kappa(x, x') = \frac{1}{2} \left[\int p(w) e^{iw(x-x')} dw + \int p(w) e^{-iw(x-x')} dw \right] = \int p(w) e^{iw(x-x')} dw. \quad (10)$$

Again, by letting $r = x - x'$, we find that we recover the spectral density decomposition of a stationary process given by the Wiener–Khinchin theorem. A detailed derivation can be found in App. A.2.

Triangle wave activation Inspired by the success of piecewise linear activation functions (*e.g.*, ReLU [36], leaky ReLU [54], PReLU [17]), we show that the triangle wave, a periodic piecewise linear function, can be used instead of sinusoidal activations. The triangle wave is given by:

$$\psi(x) = \frac{4}{p} \left(x - \frac{p}{2} \left\lfloor \frac{2x}{p} + \frac{1}{2} \right\rfloor \right) (-1)^{\lfloor \frac{2x}{p} + \frac{1}{2} \rfloor}, \quad (11)$$

where p is the period and $\lfloor \bullet \rfloor$ denotes the floor function. By considering a period of $p = 2\pi$, assuming a uniform prior on the biases, $b \sim \text{Uniform}(-\pi, \pi)$, and appropriate rescaling, we get the activation

$$\sigma_{\text{triangle}}(x) = \frac{\pi}{2\sqrt{2}} \left(x - \pi \left\lfloor \frac{x}{\pi} + \frac{1}{2} \right\rfloor \right) (-1)^{\lfloor \frac{x}{\pi} + \frac{1}{2} \rfloor}, \quad (12)$$

for which we obtain a direct correspondence of the network weight priors to the spectral density. As shown in the derivations in App. A.3, we find that we again recover the spectral density decomposition of a stationary process given by the Wiener–Khinchin theorem.

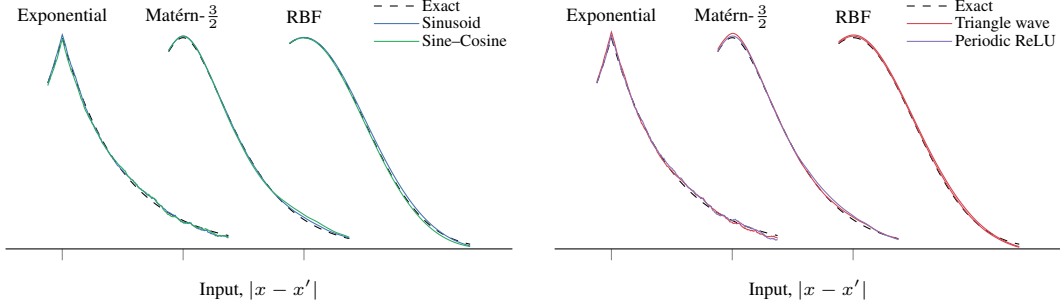


Figure 4: Covariance functions calculated by MC integration with 5000 samples and compared to their exact dashed counterparts (peaks shifted for clarity). Regardless of the type of periodic activation function used, we can recover the behaviour of the stationary kernels (see also Fig. 8a).

Periodic ReLU activation To go even further, we define a piecewise linear periodic activation function with a repeating rectified linear pattern, which we call the periodic ReLU function. It can be defined in terms of the sum of two triangle waves, with the second one being shifted by $1/4$ of a period. The resulting periodic function is piecewise linear and defined as:

$$\psi(x) = \frac{8}{\pi^2} \left(\left(\left(x + \frac{\pi}{2} \right) - \pi \left\lfloor \frac{x + \frac{\pi}{2}}{\pi} + \frac{1}{2} \right\rfloor \right) (-1)^{\lfloor \frac{x + \frac{\pi}{2}}{\pi} + \frac{1}{2} \rfloor} + \left(x - \pi \left\lfloor \frac{x}{\pi} + \frac{1}{2} \right\rfloor \right) (-1)^{\lfloor \frac{x}{\pi} + \frac{1}{2} \rfloor} \right), \quad (13)$$

assuming a period of $p = 2\pi$. It is again possible to obtain a correspondence between the network weight prior and the spectral density by considering a weighted version of the equation above. In particular, we show in App. A.4 that from the following weighted periodic ReLU activation function,

$$\sigma_{\text{pReLU}}(x) = \frac{\pi}{4} \left(\left(\left(x + \frac{\pi}{2} \right) - \pi \left\lfloor \frac{x + \frac{\pi}{2}}{\pi} + \frac{1}{2} \right\rfloor \right) (-1)^{\lfloor \frac{x + \frac{\pi}{2}}{\pi} + \frac{1}{2} \rfloor} + \left(x - \pi \left\lfloor \frac{x}{\pi} + \frac{1}{2} \right\rfloor \right) (-1)^{\lfloor \frac{x}{\pi} + \frac{1}{2} \rfloor} \right), \quad (14)$$

we again recover the spectral density decomposition of a stationary process given by the Wiener-Khinchin theorem, providing a direct connection between the prior on the weights and the spectral density. Note that, choosing a piecewise linear periodic activation function has potential computational benefits compared to sinusoidal activation functions and can help prevent vanishing gradients.

3.3 Kernel Functions

We have established that it is possible to obtain a direct correspondence of the prior on the weights and the spectral density of a stationary covariance function by using periodic activation functions in random neural networks. In App. B we show that by placing a Student- t distribution on the weights with degrees of freedom of $u = 2\nu$ we recover the spectral density of the Matérn family, *i.e.*,

$$p(w) = \frac{\Gamma(\frac{u+1}{2})}{\sqrt{u\pi}\Gamma(\frac{u}{2})} \left(1 + \frac{w^2}{u} \right)^{-\frac{u+1}{2}} = \frac{1}{2\pi} 2\sqrt{\pi} \frac{\Gamma(\nu + \frac{1}{2})}{\Gamma(\nu)} (2\nu)^\nu (2\nu + w^2)^{-(\nu + \frac{1}{2})} = \frac{1}{2\pi} S_{\text{Mat.}}(w), \quad (15)$$

where $p(w)$ denotes the probability density function of a Student- t distribution and $S_{\text{Mat.}}(w)$ denotes the spectral density of the Matérn family. This means that a Student- t prior on the weights in combination with an appropriately scaled periodic activation function corresponds directly to a prior in the function space with Matérn covariance structure. Fig. 4 verifies this result and shows that we recover the exact covariance function (dashed) for various examples from the Matérn family by Monte Carlo (MC) integration (5000 samples) with all of the discussed periodic activation functions.

Recall that the Matérn family contains the exponential kernel ($\nu = 1/2$) and the RBF Kernel ($\nu = \infty$) as special cases. Similarly, the Student- t distribution has the Cauchy ($u = 1$) and the Normal distribution ($u = \infty$) as limiting cases, resulting in correspondence to the respective special cases in the Matérn family. Table 2 in App. B summarises the set of priors on the weights that correspond to the spectral density of kernel functions in the Matérn family. This correspondence is exact for the sinusoidal and sine-cosine activations. For the triangle wave and periodic ReLU activations, the obtained correspondence is approximate, and the introduced approximation error is analyzed in detail in App. A.

Table 1: Examples of UCI regression tasks, showing the globally stationary NN model directly gives competitive RMSE and for most data sets also improved mean negative log predictive density (NLPD) compared to non-stationary and locally stationary NN models. KFAC Laplace was used as the inference method. High std is due to variability in 10-fold-cv splits of the small data sets, not method performance.

(n, d) (c, n_{batch})	BOSTON (506, 12) (1, 50)		CONCRETE (1030, 5) (1, 50)		AIRFOIL (1503, 5) (1, 50)		ELEVATORS (16599, 18) (1, 500)	
	NLPD	RMSE	NLPD	RMSE	NLPD	RMSE	NLPD	RMSE
ReLU	0.51±0.32	0.37±0.07	0.78±0.16	0.48±0.04	0.51±0.53	0.41±0.21	0.38±0.03	0.35±0.01
loc RBF	0.52±0.30	0.37±0.08	0.78±0.22	0.44±0.05	0.10±0.15	0.26±0.03	0.41±0.04	0.35±0.01
glob RBF (sin)	0.42±0.34	0.36±0.07	0.74±0.15	0.49±0.05	0.14±0.17	0.29±0.05	0.38±0.03	0.35±0.01
glob RBF (prelu)	0.39±0.30	0.36±0.07	0.74±0.14	0.49±0.04	0.05±0.12	0.26±0.03	0.74±0.73	0.46±0.21
loc Mat-3/2	0.71±0.38	0.40±0.08	0.84±0.28	0.42±0.04	0.11±0.18	0.26±0.03	0.43±0.04	0.35±0.01
glob Mat-3/2 (sin)	0.43±0.27	0.39±0.08	0.73±0.16	0.49±0.05	0.07±0.15	0.27±0.03	0.37±0.03	0.35±0.01
glob Mat-3/2 (prelu)	0.38±0.22	0.38±0.08	0.72±0.18	0.48±0.05	0.08±0.12	0.27±0.03	0.39±0.03	0.36±0.01

4 Experiments

To assess the performance of stationarity-inducing activation functions, we compared the in-domain and out-of-domain predictive uncertainty to non-stationary and locally stationary models on various benchmark data sets. In all experiments, the compared models differ only by the activation function and the respective weight priors of the last hidden layer of the network. Replacing the prior effects the initialization of the NN weights and the training objective, as we maximize the log joint density. A detailed description of the experimental setup is available in App. D. The illustrative toy BNN examples are implemented using Turing.jl [14], GP regression results use GPflow [33], and all other experiments are implemented using PyTorch [41].

Illustrative toy examples Fig. 1 shows predictive densities for non-stationary, locally stationary, and globally stationary activation functions on the banana classification task. The top row illustrates the predictive densities of infinite-width BNNs (GP), the bottom row shows corresponding results for a single hidden layer BNN using 30 hidden units. We observe that global stationarity-inducing activation functions revert to the prior outside the data, leading to conservative behaviour (high uncertainty) for out-of-domain samples. Moreover, we see that the finite-width BNNs result in similar behaviour to their infinite-width counterpart, while locally stationary activation functions in finite-width BNNs exhibit a slower reversion to the mean than their infinite-width corresponding GPs. Additionally, we include a 1D toy regression study that highlights the differences between different prior assumptions encoded by choice of the activation function. Fig. 2 shows the corresponding prior covariance as well as posterior predictions for the infinite-width (GP) model. We replicated the experiment with a finite-width network and observed that the behaviour translates to finite width (see Fig. 8 in App. D.1).

UCI benchmarks Table 1 shows results on UCI [8] regression data sets comparing deep neural networks with ReLU, locally stationary RBF [60], and locally stationary Matérn-3/2 [34] against global stationary models. An extended results table can be found in App. D.2 and additional results

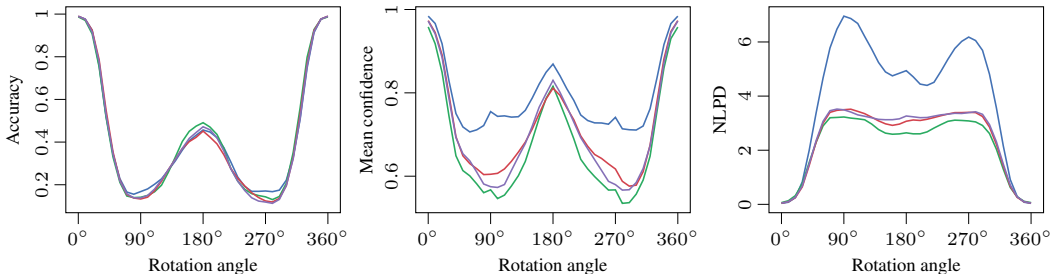


Figure 5: Rotated MNIST: The models have been trained on unrotated digits. The test-set digits are rotated at test time to show the sensitivity of the trained model to perturbations. All models perform equally in terms of accuracy, while ReLU (—) shows overconfidence in terms of mean confidence and NLPD. The stationary RBF models (— local, — sin, — sin-cos) capture uncertainty.

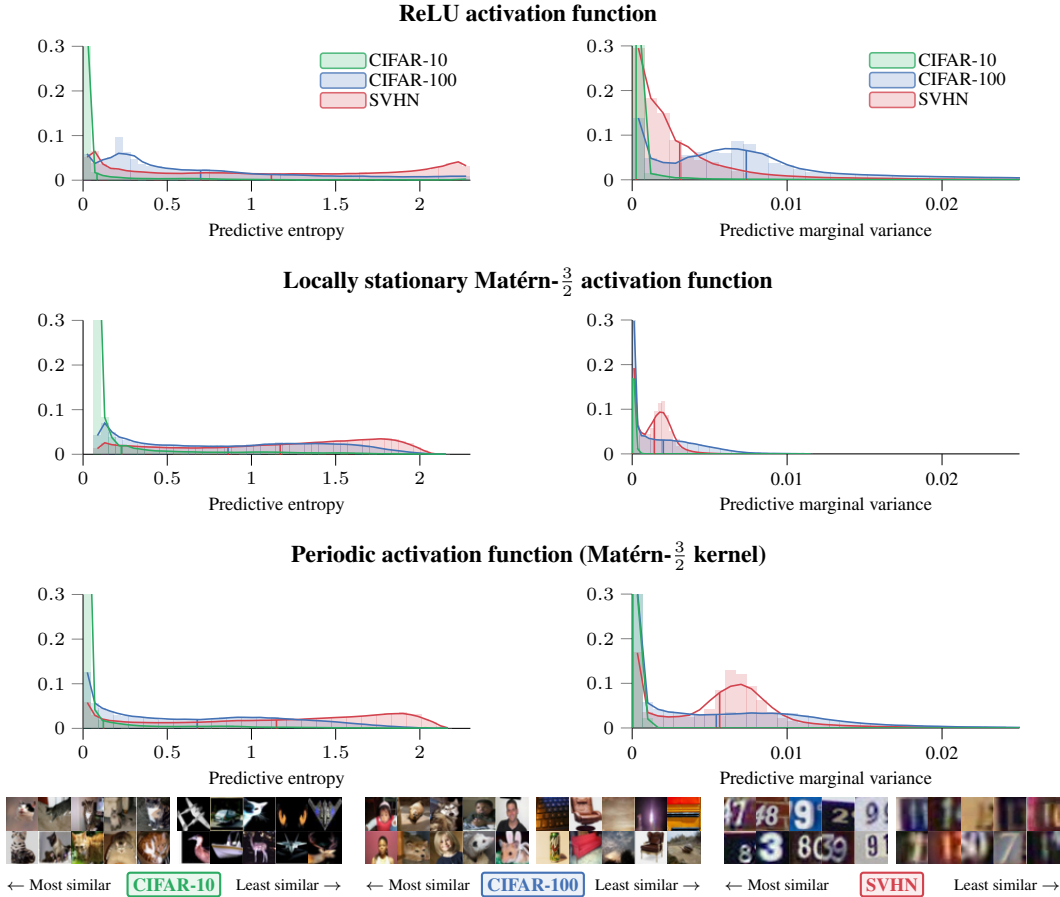


Figure 6: OOD detection experiment results for models trained on CIFAR-10 and tested on CIFAR-10, CIFAR-100, and SVHN. Top rows show predictive entropy and predictive marginal variance histograms of test images for in-domain and OOD data sets. Top to bottom: ReLU activation function, local stationary Matérn- $\frac{3}{2}$ activation function [34], and sinusoidal activation function that induces a globally stationary Matérn- $\frac{3}{2}$ model. The last row shows sample images from each test set: left-side images with the lowest entropy/highest confidence and right-side images with the highest entropy/lowest confidence. See App. D.5 for histograms for more models.

on UCI classification tasks in App. D.3. Table 1 lists root mean square error (RMSE) and negative log predictive density (NLPD), which captures the predictive uncertainty, while the RMSE only accounts for the mean. Global stationary models provide better estimates of the target distribution in all cases while obtaining comparable RMSEs. It is important to note that the large standard deviations in Table 1 are due to the small number of data points and the fact that some splits in the 10-fold CV end up being harder than others. The posterior inference is performed using KFAC Laplace [45].

Detection of distribution shift with rotated MNIST Fig. 5 demonstrates the predictive behaviour of different activation functions under covariate shift. We evaluate the predictive accuracy, mean confidence of the predicted class, and NLPD on MNIST [25] for different rotations of the input. Models are trained on unrotated digits using KFAC Laplace [45]. The results indicate that all models obtain similar accuracy results, while only local and global stationary models do not result in over-confident uncertainty estimates. For an ideally calibrated model, the mean confidence would decrease as low as the accuracy curve when the digits are rotated, keeping the NLPD values as low as possible.

Out-of-distribution detection using CIFAR-10, CIFAR-100, and SVHN Fig. 6 shows model performance on OOD detection in image classification for ReLU, locally stationary Matérn- $\frac{3}{2}$, and globally stationary Matérn- $\frac{3}{2}$ models. The models have been trained using SWAG [29] on CIFAR-10 [23], and tested on CIFAR-10, CIFAR-100 [23], and SVHN [39] test set images. Both CIFAR-100 (more similar) and SVHN (more dissimilar to CIFAR-10) images are OOD data, and the

models should show high uncertainties for the respective test images. We use two metrics to measure model uncertainty: predictive entropy and predictive marginal variance. Predictive entropy captures uncertainty present in the predicted mean class weights, while the predictive marginal variance captures uncertainty related to the variability in the predicted class weights. From these two metrics, the predictive marginal variance could be more suitable as an OOD detection metric, as predictive entropy can justifiably give high values for some in-distribution samples, for example, those that the model confidently predicts being in between two known classes.

The histograms of predictive entropies for different test sets show that all models can separate between in-distribution and OOD data to some extent, and all models consider SVHN more OOD than CIFAR-100, which is intuitive as CIFAR-100 resembles CIFAR-10 more. Also, the predictive marginal variance histograms show that the models have higher variance on OOD data compared to in-distribution data. However, the ReLU model considers CIFAR-100 more OOD than SVHN and the locally stationary Matérn- $3/2$ model has overall relatively small predictive marginal variance values for all data sets. We consider predictive marginal variance a better metric for OOD detection than predictive entropy, as in-distribution samples that are hard to classify are expected to have high predictive entropy, not necessarily allowing the detection of OOD samples on this metric. See Fig. 14 in App. D.5 for results on different models, and Table 8 in App. D.5 for numerical results showing the area under the receiver operating characteristic curve and the area under the precision-recall curve for the OOD detection experiment.

5 Discussion and Conclusions

We have shown that *periodic* activation functions in Bayesian neural networks (BNNs) establish a direct connection between the prior on the network weights and the spectral density of the limiting stationary process. This link goes beyond the Fourier (sinusoidal) basis, which we have illustrated by deriving the correspondence also for the triangle wave and a new periodic variant of the ReLU activation function. Moreover, we have shown that for BNNs with a periodic activation function, placing a Student- t distribution on the network weights corresponds to a prior in the function space with Matérn covariance structure. This correspondence is exact for the sinusoidal and sin-cos activations and approximate for the triangle and periodic ReLU activations.

Our work can help build neural network models that are more robust and less vulnerable to OOD data—occurring either naturally or maliciously. As demonstrated in the experiments, the modelling assumptions have practical importance in reducing sensitivity to input shift. Perturbation of inputs can be captured in the last layer of a deep model, and the principled choice of *a priori* stationarity has shown to be effective based on the experiments. Using periodic activation functions in BNNs induces *global* stationarity, *i.e.*, the model is not only locally translation-invariant, which induces conservative behaviour across the input domain. The resulting model reverts to the prior for out-of-distribution (OOD) samples, resulting in well-specified uncertainties.

In contrast to models with non-stationary or locally stationary activations, optimising and performing approximate inference in models with periodic activation functions has proven to be more challenging. In particular, we found that the uncertainty over the bias terms is often not accurately estimated when using KFAC Laplace or SWAG, which required us to use a relatively large number of hidden units. However, the experiments using dynamic HMC indicate that the number of hidden units can be drastically reduced using a more accurate approximate inference scheme, as seen in Fig. 1 and Fig. 11 in App. D.1.

The codes and data to replicate the results are available under MIT license at <https://github.com/AaltoML/PeriodicBNN>.

Acknowledgments and Disclosure of Funding

We acknowledge the computational resources provided by the Aalto Science-IT project. This research was supported by the Academy of Finland grants 324345 and 339730, and Saab Finland Oy. We thank William J. Wilkinson and the anonymous reviewers for feedback on the manuscript.

References

- [1] L. Aitchison. A statistical theory of cold posteriors in deep neural networks. In *Proceedings of the International Conference on Learning Representations (ICLR)*, 2021.
- [2] E. J. Candès. Harmonic analysis of neural networks. *Applied and Computational Harmonic Analysis*, 6(2): 197–218, 1999.
- [3] Y. Cho and L. K. Saul. Kernel methods for deep learning. In *Proceedings of Advances in Neural Information Processing Systems (NIPS)*, pages 342–350. Curran Associates, Inc., 2009.
- [4] C. Cortes and V. Vapnik. Support-vector networks. *Machine Learning*, 20(3):273–297, 1995.
- [5] N. A. Cressie. *Statistics for Spatial Data*. Wiley series in probability and mathematical statistics. Wiley-Interscience, 1991.
- [6] G. Da Prato and J. Zabczyk. *Stochastic Equations in Infinite Dimensions*, volume 45 of *Encyclopedia of Mathematics and its Applications*. Cambridge University Press, 1992.
- [7] A. G. de G. Matthews, J. Hron, M. Rowland, R. E. Turner, and Z. Ghahramani. Gaussian process behaviour in wide deep neural networks. In *Proceedings of the International Conference on Learning Representations (ICLR)*, 2018.
- [8] D. Dua and C. Graff. UCI machine learning repository, 2017. URL <http://archive.ics.uci.edu/ml>.
- [9] A. Y. Foong, D. R. Burt, Y. Li, and R. E. Turner. On the expressiveness of approximate inference in Bayesian neural networks. In *Proceedings of Advances in Neural Information Processing Systems (NeurIPS)*, pages 15897–15908. Curran Associates, Inc., 2020.
- [10] V. Fortuin, A. Garriga-Alonso, F. Wenzel, G. Rätsch, R. E. Turner, M. van der Wilk, and L. Aitchison. Bayesian neural network priors revisited. In *Third Symposium on Advances in Approximate Bayesian Inference*, 2021.
- [11] D. Gabor. Theory of communication part 1: The analysis of information. *Journal of the Institution of Electrical Engineers—Part III: Radio and Communication Engineering*, 93(26):429–441, 1946.
- [12] Y. Gal and Z. Ghahramani. Dropout as a Bayesian approximation: Representing model uncertainty in deep learning. In *Proceedings of the International Conference on Machine Learning (ICML)*, volume 48 of *Proceedings of Machine Learning Research*, pages 1050–1059. PMLR, 2016.
- [13] A. R. Gallant and H. White. There exists a neural network that does not make avoidable mistakes. In *Proceedings of International Conference on Neural Networks (ICNN)*, pages 657–664, 1988.
- [14] H. Ge, K. Xu, and Z. Ghahramani. Turing: A language for flexible probabilistic inference. In *Proceedings of the International Conference on Artificial Intelligence and Statistics (AISTATS)*, volume 84 of *Proceedings of Machine Learning Research*, pages 1682–1690. PMLR, 2018.
- [15] M. G. Genton. Classes of kernels for machine learning: A statistics perspective. *Journal of Machine Learning Research*, 2:299–312, 2001.
- [16] I. Goodfellow, Y. Bengio, and A. Courville. *Deep Learning*. MIT Press, 2016.
- [17] K. He, X. Zhang, S. Ren, and J. Sun. Delving deep into rectifiers: Surpassing human-level performance on imagenet classification. In *Proceedings of the International Conference on Computer Vision (ICCV)*, pages 1026–1034, 2015.
- [18] M. Hein, M. Andriushchenko, and J. Bitterwolf. Why ReLU networks yield high-confidence predictions far away from the training data and how to mitigate the problem. In *Proceedings of the IEEE Conference on Computer Vision and Pattern Recognition (CVPR)*, pages 41–50, 2019.
- [19] J. Hensman, N. Durrande, and A. Solin. Variational Fourier features for Gaussian processes. *Journal of Machine Learning Research*, 18:1–52, 2018.
- [20] T. Hofmann, B. Schölkopf, and A. J. Smola. Kernel methods in machine learning. *The Annals of Statistics*, pages 1171–1220, 2008.
- [21] A. Jacot, F. Gabriel, and C. Hongler. Neural tangent kernel: Convergence and generalization in neural networks. In *Advances in Neural Information Processing Systems 31*, pages 8571–8580. Curran Associates, Inc., 2018.

- [22] A. Kristiadi, M. Hein, and P. Hennig. Being bayesian, even just a bit, fixes overconfidence in ReLU networks. In *Proceedings of the International Conference on Machine Learning (ICML)*, volume 119 of *Proceedings of Machine Learning Research*, pages 5436–5446. PMLR, 2020.
- [23] A. Krizhevsky. Learning multiple layers of features from tiny images. *University of Toronto*, 2012.
- [24] M. Lázaro-Gredilla, J. Quiñero-Candela, C. E. Rasmussen, and A. R. Figueiras-Vidal. Sparse spectrum Gaussian process regression. *Journal of Machine Learning Research*, 11:1865–1881, 2010.
- [25] Y. LeCun, C. Cortes, and C. J. Burges. The MNIST database of handwritten digits, 1998. URL <http://yann.lecun.com/exdb/mnist/>.
- [26] J. Lee, Y. Bahri, R. Novak, S. S. Schoenholz, J. Pennington, and J. Sohl-Dickstein. Deep neural networks as Gaussian processes. In *International Conference on Learning Representations (ICLR)*, 2018.
- [27] J. Lee-Thorp, J. Ainslie, I. Eckstein, and S. Ontañón. Fnet: Mixing tokens with Fourier transforms. *ArXiv preprint arXiv:1401.5508*, 2021.
- [28] L. Loomis. *An Introduction to Abstract Harmonic Analysis*. D. van Nostrand Company, Inc., New York, 1954.
- [29] W. J. Maddox, P. Izmailov, T. Garipov, D. P. Vetrov, and A. G. Wilson. A simple baseline for Bayesian uncertainty in deep learning. In *Advances in Neural Information Processing Systems 32 (NeurIPS)*, pages 13132–13143. Curran Associates, Inc., 2019.
- [30] H. Maennel. Uncertainty estimates and out-of-distribution detection with Sine Networks. In *ICML 2019 Workshop on Uncertainty and Robustness in Deep Learning*, 2019.
- [31] G. Marcus. The next decade in AI: Four steps towards robust artificial intelligence. *arXiv preprint arXiv:2002.06177*, 2020.
- [32] B. Matérn. Spatial variation: Stochastic models and their applications to some problems in forest surveys and other sampling investigations. *Meddelanden från statens skogsforskningsinstitut*, 49:1–144, 1960.
- [33] A. G. d. G. Matthews, M. van der Wilk, T. Nickson, K. Fujii, A. Boukouvalas, P. León-Villagrà, Z. Ghahramani, and J. Hensman. GPflow: A Gaussian process library using TensorFlow. *Journal of Machine Learning Research*, 18(40):1–6, 2017.
- [34] L. Meronen, C. Irwanto, and A. Solin. Stationary activations for uncertainty calibration in deep learning. In *Proceedings of Advances in Neural Information Processing Systems (NeurIPS)*, pages 2338–2350. Curran Associates, Inc., 2020.
- [35] P. Morales-Alvarez, D. Hernández-Lobato, R. Molina, and J. M. Hernández-Lobato. Activation-level uncertainty in deep neural networks. In *Proceedings of the International Conference on Learning Representations (ICLR)*, 2021.
- [36] V. Nair and G. E. Hinton. Rectified linear units improve restricted boltzmann machines. In *Proceedings of the International Conference on Machine Learning (ICML)*, pages 807–814. Omnipress, 2010.
- [37] E. T. Nalisnick, J. Gordon, and J. M. Hernández-Lobato. Predictive complexity priors. In *Proceedings of the International Conference on Artificial Intelligence and Statistics (AISTATS)*, volume 130 of *Proceedings of Machine Learning Research*, pages 694–702. PMLR, 2021.
- [38] R. M. Neal. *Bayesian Learning for Neural Networks*. PhD thesis, University of Toronto, Toronto, Canada, 1995.
- [39] Y. Netzer, T. Wang, A. Coates, A. Bissacco, B. Wu, and A. Y. Ng. Reading digits in natural images with unsupervised feature learning. In *NIPS Workshop on Deep Learning and Unsupervised Feature Learning*. 2011. URL <http://ufldl.stanford.edu/housenumbers>.
- [40] A. Papoulis. *Probability, Random Variables, and Stochastic Processes*. McGraw-Hill, New York, 1991.
- [41] A. Paszke, S. Gross, F. Massa, A. Lerer, J. Bradbury, G. Chanan, T. Killeen, Z. Lin, N. Gimelshein, L. Antiga, A. Desmaison, A. Kopf, E. Yang, Z. DeVito, M. Raison, A. Tejani, S. Chilamkurthy, B. Steiner, L. Fang, J. Bai, and S. Chintala. Pytorch: An imperative style, high-performance deep learning library. In *Proceedings of Advances in Neural Information Processing Systems (NeurIPS)*, pages 8024–8035. Curran Associates, Inc., 2019.

- [42] T. Pearce, R. Tsuchida, M. Zaki, A. Brintrup, and A. Neely. Expressive priors in Bayesian neural networks: Kernel combinations and periodic functions. In *Proceedings of the Conference on Uncertainty in Artificial Intelligence (UAI)*, volume 115 of *Proceedings of Machine Learning Research*, pages 134–144. PMLR, 2019.
- [43] A. Rahimi and B. Recht. Random features for large-scale kernel machines. In *Proceedings of Advances in Neural Information Processing Systems (NeurIPS)*, pages 1177–1184. Curran Associates, Inc., 2008.
- [44] C. E. Rasmussen and C. K. I. Williams. *Gaussian Processes for Machine Learning*. MIT Press, Cambridge, MA, 2006.
- [45] H. Ritter, A. Botev, and D. Barber. A scalable Laplace approximation for neural networks. In *International Conference on Learning Representations (ICLR)*, 2018.
- [46] J. Schmidhuber. Deep learning in neural networks: An overview. *Neural Networks*, 61:85–117, 2015.
- [47] V. Sitzmann, J. N. P. Martel, A. W. Bergman, D. B. Lindell, and G. Wetzstein. Implicit neural representations with periodic activation functions. In *Proceedings of Advances in Neural Information Processing Systems (NeurIPS)*, pages 7462–7473. Curran Associates, Inc., 2020.
- [48] A. Solin and S. Särkkä. Hilbert space methods for reduced-rank Gaussian process regression. *Statistics and Computing*, 30(2):419–446, 2020.
- [49] M. L. Stein. *Interpolation of Spatial Data*. Springer Series in Statistics. Springer, New York, 1999.
- [50] S. Sun, G. Zhang, J. Shi, and R. B. Grosse. Functional variational Bayesian neural networks. In *Proceedings of the International Conference on Learning Representations (ICLR)*, 2019.
- [51] D. J. Sutherland and J. G. Schneider. On the error of random Fourier features. In *Proceedings of the Conference on Uncertainty in Artificial Intelligence (UAI)*, pages 862–871. AUAI Press, 2015.
- [52] C. Szegedy, W. Liu, Y. Jia, P. Sermanet, S. Reed, D. Anguelov, D. Erhan, V. Vanhoucke, and A. Rabinovich. Going deeper with convolutions. In *Proceedings of the IEEE Conference on Computer Vision and Pattern Recognition (CVPR)*, pages 1–9, 2015.
- [53] M. Tancik, P. Srinivasan, B. Mildenhall, S. Fridovich-Keil, N. Raghavan, U. Singhal, R. Ramamoorthi, J. Barron, and R. Ng. Fourier features let networks learn high frequency functions in low dimensional domains. In *Proceedings of Advances in Neural Information Processing Systems (NeurIPS)*, pages 7537–7547. Curran Associates, Inc., 2020.
- [54] R. Tsuchida, F. Roosta, and M. Gallagher. Invariance of weight distributions in rectified MLPs. In *Proceedings of the International Conference on Machine Learning (ICML)*, volume 80 of *Proceedings of Machine Learning Research*, pages 4995–5004. PMLR, 2018.
- [55] D. Ulmer and G. Cinà. Know your limits: Uncertainty estimation with ReLU classifiers fails at reliable OOD detection. In *Proceedings of the Thirty-Seventh Conference on Uncertainty in Artificial Intelligence*, volume 161 of *Proceedings of Machine Learning Research*, pages 1766–1776. PMLR, 2021.
- [56] M. Uteuliyeva, A. Zhumekenov, R. Takhanov, Z. Assylbekov, A. J. Castro, and O. Kabdolov. Fourier neural networks: A comparative study. *Intelligent Data Analysis*, 24(5):1107–1120, 2020.
- [57] F. Wenzel, K. Roth, B. S. Veeling, J. Świątkowski, L. Tran, S. Mandt, J. Snoek, T. Salimans, R. Jenatton, and S. Nowozin. How good is the Bayes posterior in deep neural networks really? In *Proceedings of the International Conference on Machine Learning (ICML)*, volume 119 of *Proceedings of Machine Learning Research*, pages 10248–10259. PMLR, 2020.
- [58] N. Wiener. Generalized harmonic analysis. *Acta Mathematica*, 55:117–258, 1930.
- [59] C. K. I. Williams. Computing with infinite networks. In *Proceedings of Advances in Neural Information Processing Systems (NIPS)*, pages 295–301. MIT Press, 1997.
- [60] C. K. I. Williams. Computation with infinite neural networks. *Neural Computation*, 10(5):1203–1216, 1998.
- [61] K. Wong, C. Leung, and S. Chang. Handwritten digit recognition using multi-layer feedforward neural networks with periodic and monotonic activation functions. In *Proceedings of International Conference on Pattern Recognition (ICNN)*, pages 106–109, 2002.
- [62] I.-C. Yeh. Modeling of strength of high-performance concrete using artificial neural networks. *Cement and Concrete Research*, 28:1797–1808, 1998.

Supplementary Material: Periodic Activation Functions Induce Stationarity

This supplementary document is organized as follows. App. A includes further details and derivations for the periodic activation functions in the Methods section of the main paper. App. B provides a full derivation of the correspondence between the Student- t prior and Matérn family under periodic activation functions. App. C presents and discusses further links to existing work. App. D includes details on the experiments, baseline methods, data sets, and additional tables and result plots.

A Derivations for Activation Functions

In this section we will introduce the detailed derivations for the activation functions presented in the main text. In each derivation, we start from the definition of the covariance function of a random single-layer neural network given as:

$$\kappa(x, x') = \int \int p(w) p(b) \sigma(wx + b) \sigma(wx' + b) db dw, \quad (16)$$

where $\sigma(\cdot)$ denotes the activation function and $p(w)$ and $p(b)$ the priors over weights and biases respectively.

A.1 Sinusoidal Activation Function

Let the activation function $\sigma(\cdot)$ and prior $p(b)$ take the following form:

$$\sigma(x) = \sqrt{2} \sin(x), \quad (17)$$

$$p(b) = \text{Uniform}(-\pi, \pi). \quad (18)$$

Then the covariance function $\kappa(x, x')$ from Eq. (16) can now be written as:

$$\kappa(x, x') = \int p(w) \int_{-\pi}^{\pi} \frac{1}{\pi} \sin(wx + b) \sin(wx' + b) db dw. \quad (19)$$

The inner integral (over b) can now be solved by considering that $\sin(x) \sin(y) = \frac{1}{2}[\cos(x - y) - \cos(x + y)]$, *i.e.*,

$$\begin{aligned} & \int_{-\pi}^{\pi} \sin(wx + b) \sin(wx' + b) db \\ &= \int_{-\pi}^{\pi} \frac{\cos(wx + b - wx' - b) - \cos(wx + b + wx' + b)}{2} db \\ &= \frac{1}{2} \int_{-\pi}^{\pi} \cos(w(x - x')) - \cos(w(x + x') + 2b) db \\ &= \pi \cos(w(x - x')). \end{aligned} \quad (20)$$

Plugging the above back into Eq. (19) gives us:

$$\kappa(x, x') = \int p(w) \cos(w(x - x')) dw, \quad (21)$$

which, by application of Euler's formula $\cos(z) = \frac{1}{2}(e^{iz} + e^{-iz})$, can be written as:

$$\kappa(x, x') = \frac{1}{2} \int p(w) e^{iw(x-x')} dw + \frac{1}{2} \int p(w) e^{-iw(x-x')} dw. \quad (22)$$

Since the integration is over the entire real line we can do a change of variables $w = -w$ in the second integral and by assuming a symmetric prior on w , we obtain

$$\begin{aligned}\kappa(x, x') &= \frac{1}{2} \int p(w) e^{iw(x-x')} dw + \frac{1}{2} \int p(-w) e^{iw(x-x')} dw \\ &= \int p(w) e^{iw(x-x')} dw.\end{aligned}\quad (23)$$

By letting $r = x - x'$, we find that we recover the spectral density decomposition of a stationary process given by the Wiener–Khinchin theorem, *i.e.*,

$$\kappa(r) = \int p(w) e^{iwr} dw, \quad (24)$$

where $p(w) = \frac{1}{2\pi} S(w)$, which was to be shown.

A.2 Sine–Cosine Activation Function

Let us assume a bias-free random single-layer neural network. Following Eq. (16), in the infinite limit, the corresponding covariance function would take the form:

$$\kappa(x, x') = \int p(w) \sigma(wx) \sigma(wx') dw. \quad (25)$$

Let the activation function be given as:

$$\sigma(x) = \sin(x) + \cos(x). \quad (26)$$

This gives the covariance function in the form

$$\begin{aligned}\kappa(x, x') &= \int p(w) [\sin(wx) + \cos(wx)] [\sin(wx') + \cos(wx')] dw \\ &= \int p(w) \sin(w(x+x')) dw + \int p(w) \cos(w(x-x')) dw.\end{aligned}\quad (27)$$

By application of Euler’s formula we get

$$\begin{aligned}\kappa(x, x') &= \frac{1}{2} \left[\int p(w) e^{iw(x-x')} dw + \int p(w) e^{-iw(x-x')} dw \right. \\ &\quad \left. + \int p(w) i e^{iw(x+x')} dw - \int p(w) i e^{-iw(x+x')} dw \right],\end{aligned}\quad (28)$$

where under assumption that $p(w)$ is symmetric and has support on the entire real line the above reduces to:

$$\begin{aligned}\kappa(x, x') &= \frac{1}{2} \left[\int p(w) e^{iw(x-x')} dw + \int p(w) e^{-iw(x-x')} dw \right] \\ &= \int p(w) e^{iw(x-x')} dw,\end{aligned}\quad (29)$$

where the last step follows from application of the change of variables and the symmetry of $p(w)$. Again, by letting $r = x - x'$, we find that we recover the spectral density decomposition of a stationary process given by the Wiener–Khinchin theorem, *i.e.*,

$$\kappa(r) = \int p(w) e^{iwr} dw \quad (30)$$

confirming the statement in the main paper.

A.3 Triangle Wave Activation

The triangle wave is a periodic, piecewise linear function and it can be written in a parametric form as

$$\psi(x) = \frac{4}{p} \left(x - \frac{p}{2} \left[\frac{2x}{p} + \frac{1}{2} \right] \right) (-1)^{\lfloor \frac{2x}{p} + \frac{1}{2} \rfloor}, \quad (31)$$

where p is the period of the triangle wave. In the following derivation we will assume that $p = 2\pi$. For analysis, we note that the Fourier series approximation to $\psi(x)$ can be given in the following form (in the limit of n):

$$\psi(x) = \lim_{n \rightarrow \infty} \frac{8}{\pi^2} \sum_{k=0}^{n-1} (-1)^k (2k+1)^{-2} \sin((2k+1)x). \quad (32)$$

Let $\lambda_k := 2k + 1$, and let us assume the triangle wave activation function and a uniform prior on b (as in the preceding derivation):

$$\sigma(z) = \sqrt{2} \sum_{k=0}^{n-1} (-1)^k \lambda_k^{-2} \sin(\lambda_k z), \quad (33)$$

$$p(b) = \text{Uniform}(-\pi, \pi), \quad (34)$$

where n is the number of harmonics to include in the approximation and k is the harmonic label.

The covariance function $\kappa(x, x')$ is, therefore, given as:

$$\begin{aligned} \kappa(x, x') = \int p(w) \int_{-\pi}^{\pi} 2p(b) \left[\sum_{k=0}^{n-1} (-1)^k \lambda_k^{-2} \sin(\lambda_k(wx + b)) \right] \\ \left[\sum_{j=0}^{n-1} (-1)^j \lambda_j^{-2} \sin(\lambda_j(wx' + b)) \right] dw db. \end{aligned} \quad (35)$$

Now, let us solve the inner integrals by ignoring the constant terms and assuming that $k \neq j$:

$$\begin{aligned} \int_{-\pi}^{\pi} \frac{1}{\pi} \sin(\lambda_k(wx + b)) \sin(\lambda_j(wx' + b)) db \\ = \int_{-\pi}^{\pi} \frac{1}{2\pi} \cos(\lambda_k(wx + b) - \lambda_j(wx' + b)) - \cos(\lambda_k(wx + b) + \lambda_j(wx' + b)) db. \end{aligned} \quad (36)$$

By solving the definite integral above, we obtain:

$$\begin{aligned} = \frac{\sin(w(\lambda_k x - \lambda_j x')) - \sin(w(\lambda_k x - \lambda_j x')) + 2\pi(\lambda_k - \lambda_j)}{\lambda_j - \lambda_k} \\ + \frac{\sin(w(\lambda_k x + \lambda_j x')) - \sin(w(\lambda_k x + \lambda_j x')) + 2\pi(\lambda_k + \lambda_j)}{\lambda_j + \lambda_k}, \end{aligned} \quad (37)$$

where we recognise that $2\pi(\lambda_k - \lambda_j)$ will always be an even multiple of 2π , as both λ_k and λ_j are odd. Thus, the above cancels out and Eq. (35) reduces to containing only indexes $k = j$:

$$\kappa(x, x') = \int p(w) \int_{-\pi}^{\pi} 2p(b) \sum_{k=0}^{n-1} \frac{(-1)^{2k}}{\lambda_k^4} \sin(\lambda_k(wx + b)) \sin(\lambda_k(wx' + b)) dw db. \quad (38)$$

The solution to the first integral for every summand is given as:

$$\begin{aligned} \int_{-\pi}^{\pi} 2p(b) \sin(\lambda_k(wx + b)) \sin(\lambda_k(wx' + b)) db \\ = \int_{-\pi}^{\pi} \frac{1}{2\pi} \cos(w\lambda_k(x - x')) - \cos(w\lambda_k(x + y) + 2b\lambda_k) db \\ = \cos(w\lambda_k(x - x')) - \underbrace{\frac{\cos(w\lambda_k(x + x')) + 2\lambda_k\pi \sin(2\lambda_k\pi)}{\lambda_k}}_{=0}. \end{aligned} \quad (39)$$

Inserting this into the equation of the covariance function results in:

$$\kappa(x, x') = \int p(w) \sum_{k=0}^{n-1} \frac{(-1)^{2k}}{\lambda_k^4} \cos(w\lambda_k(x - x')) dw. \quad (40)$$

We now take into account that the exact solution is given when $n \rightarrow \infty$ and that $(-1)^{2k} = 1$:

$$\kappa(x, x') = \int \lim_{n \rightarrow \infty} p(w) \sum_{k=0}^{n-1} \frac{1}{\lambda_k^4} \cos(w\lambda_k(x - x')) dw. \quad (41)$$

Here we can use the dominated convergence theorem to take the limit outside of the integral. For this we have $f_n(w) = p(w) \sum_{k=0}^{n-1} \frac{1}{\lambda_k^4} \cos(w\lambda_k(x - x'))$, and we need a function $g(w)$ for which $|f_n(w)| \leq g(w)$ for all n and $\int g(w) dw < \infty$:

$$|f_n(w)| = p(w) \sum_{k=0}^{n-1} \frac{1}{(2k+1)^4} |\cos(w\lambda_k(x - x'))| \quad (42)$$

$$\leq p(w) \sum_{k=0}^{n-1} \frac{1}{(2k+1)^4} \quad (43)$$

$$\leq p(w) \sum_{k=1}^{\infty} \frac{1}{k^4} = \frac{\pi^4}{90} p(w) \quad (44)$$

Hence, by choosing $g(w) = \frac{\pi^4}{90} p(w)$ the requirements to use the dominated convergence theorem are satisfied since $\int \frac{\pi^4}{90} p(w) dw = \frac{\pi^4}{90} < \infty$.

We obtain:

$$\kappa(x, x') = \lim_{n \rightarrow \infty} \int p(w) \sum_{k=0}^{n-1} \frac{1}{\lambda_k^4} \cos(w\lambda_k(x - x')) dw. \quad (45)$$

It is also possible to write the density on the weights in Eq. (45) in the form of a mixture density (assuming the density p is in the location-scale family, which is the case for the prior distributions discussed in this paper):

$$\begin{aligned} \kappa(x, x') &= \lim_{n \rightarrow \infty} \int \sum_{k=0}^{n-1} \frac{1}{\lambda_k^4} p(w) e^{i\lambda_k w(x-x')} dw, \\ \kappa(x, x') &= \lim_{n \rightarrow \infty} \int \sum_{k=0}^{n-1} \pi_k p(w) e^{i\lambda_k w(x-x')} dw, \\ \kappa(x, x') &= \lim_{n \rightarrow \infty} \int \sum_{k=0}^{n-1} \pi_k p(w | \lambda_k) e^{iw(x-x')} dw, \end{aligned} \quad (46)$$

where $p(w | \lambda_k)$ denotes the density function of $p(w)$ with scale parameter λ_k . Let us now denote $\lim_{n \rightarrow \infty} \sum_{k=0}^{n-1} \pi_k p(w | \lambda_k)$ as $\hat{p}(w)$, *i.e.*,

$$\kappa(x, x') = \int \hat{p}(w) e^{iw(x-x')} dw. \quad (47)$$

By letting $r = x - x'$, we find that we again recover the spectral density decomposition of a stationary process given by the Wiener–Khinchin theorem, *i.e.*,

$$\kappa(r) = \int \hat{p}(w) e^{iwr} dw, \quad (48)$$

which recovers the statement in the main paper.

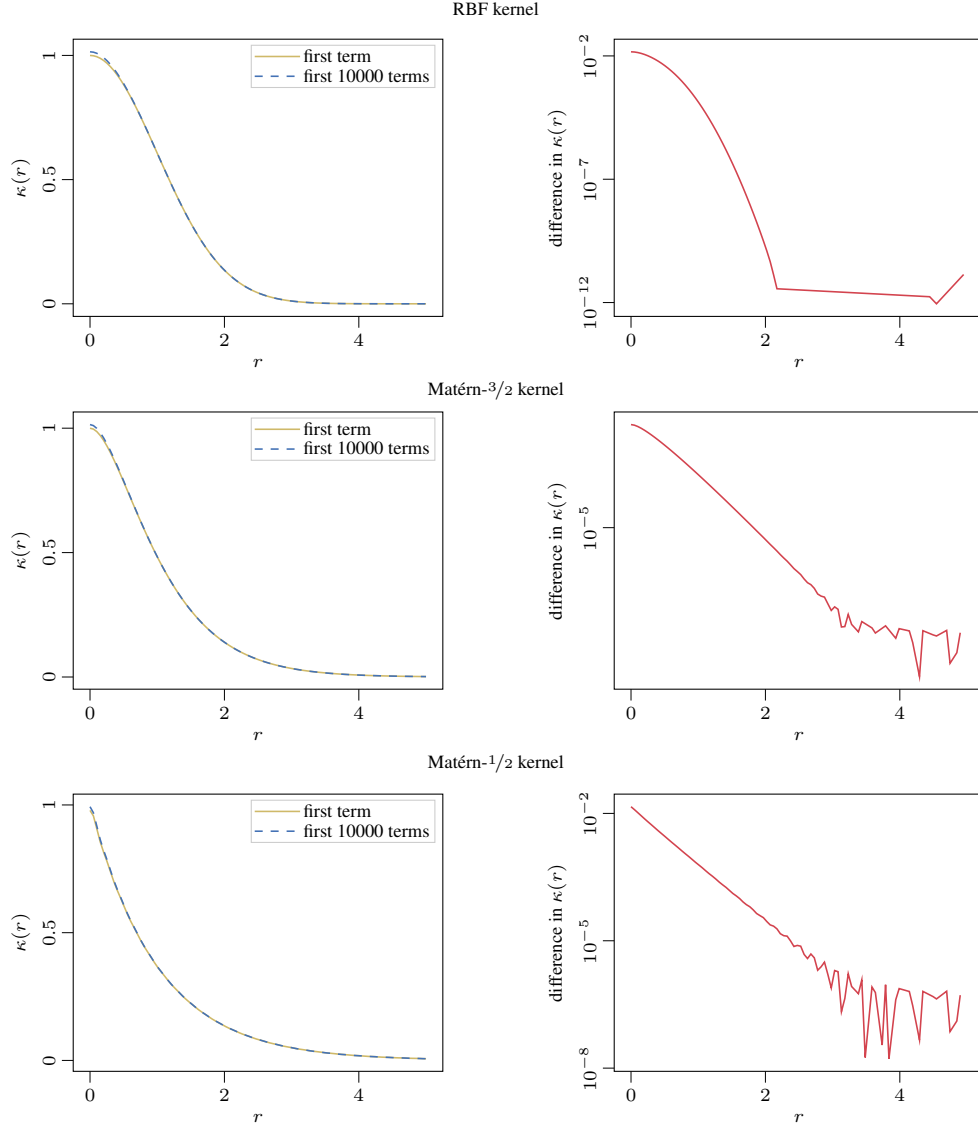


Figure 7: Numerical integration results on the error introduced by approximating the mixture in Eq. (48) using only its first component. The top row figures correspond to the RBF kernel, with $p(w)$ being standard normal distribution. The middle and bottom row figures correspond to the Matérn- $3/2$ and Matérn- $1/2$ kernels, with $p(w)$ being Student-t distribution with degrees of freedom 3 and 1 respectively. The figures on the left compare the kernel values $\kappa(r)$ from equation Eq. (45) with $r = x - x'$, while the sum has either only the first term or the 100 first terms included. The figures on the right show the difference between the curves on the left side figures on a logarithmic scale. The figures show that the error introduced by approximating the mixture in Eq. (48) using only its first component is very small when $p(w)$ is one of the distributions used in the experiments.

We again obtain a connection between the prior (in this case, a mixture) and the spectral density through the Wiener–Khinchin theorem. In this case, the spectral density also has to admit a mixture density. However, working with a mixture density as prior could be potentially challenging for inference. For this reason, in practise the mixture is approximated only using its first component, since this is a series of rapidly decreasing terms. Fig. 7 shows simulation results of the error introduced by approximating the mixture using only its first component. Based on these results the error from this approximation appears very small, when $p(w)$ is in the Matérn-class, which is the case in all experiments in this paper.

A.4 Periodic ReLU Activation

Finally, we consider a periodic function that captures the spirit of the ReLU activation function in the form of a repeating rectified linear pattern. This can be modelled as the sum of two triangle waves, the second one shifted by half a period. The resulting periodic function is piece-wise linear and defined as:

$$\psi(x) = \frac{2}{\pi} \left(\left((x + \frac{\pi}{2}) - \pi \left\lfloor \frac{(x + \frac{\pi}{2})}{\pi} + \frac{1}{2} \right\rfloor \right) (-1)^{\lfloor \frac{(x + \frac{\pi}{2})}{\pi} + \frac{1}{2} \rfloor} + \left(x - \pi \left\lfloor \frac{x}{\pi} + \frac{1}{2} \right\rfloor \right) (-1)^{\lfloor \frac{x}{\pi} + \frac{1}{2} \rfloor} \right), \quad (49)$$

assuming a period of $p = 2\pi$. In the following derivation we will again use a Fourier series approximation of a slightly differently weighted form of the periodic ReLU function as the activation function, *i.e.*,

$$\sigma(x) = \lim_{n \rightarrow \infty} \sum_{k=0}^{n-1} (-1)^k \lambda_k^{-2} \left(\sin(\lambda_k(x + \frac{\pi}{2})) + \sin(\lambda_k x) \right), \quad (50)$$

and $p(b) = \text{Uniform}(-\pi, \pi)$. Then, the covariance function is given as:

$$\begin{aligned} \kappa(x, x') = \int p(w) \int p(b) & \left[\lim_{n \rightarrow \infty} \sum_{k=0}^{n-1} (-1)^k \lambda_k^{-2} \left(\sin(\lambda_k(wx + \frac{\pi}{2} + b)) + \sin(\lambda_k(wx + b)) \right) \right] \\ & \left[\lim_{n \rightarrow \infty} \sum_{j=0}^{n-1} (-1)^j \lambda_j^{-2} \left(\sin(\lambda_j(wx' + \frac{\pi}{2} + b)) + \sin(\lambda_j(wx' + b)) \right) \right] dw db. \quad (51) \end{aligned}$$

As done previously, we will first solve the inner integral by assuming that $k \neq j$, *i.e.*,

$$\int p(b) \frac{(-1)^{k+j}}{\lambda_k^2 \lambda_j^2} \left(\sin(\lambda_k(wx + \frac{\pi}{2} + b)) + \sin(\lambda_k(wx + b)) \right) \left(\sin(\lambda_j(wx' + \frac{\pi}{2} + b)) + \sin(\lambda_j(wx' + b)) \right) db, \quad (52)$$

where we recognise that,

$$\sin(\lambda_k(wx + \frac{\pi}{2} + b)) = (-1)^k \cos(\lambda_k(wx + b)), \quad (53)$$

due to the definition of λ_k , giving us a series of definite integrals:

$$\begin{aligned} & \int_{-\pi}^{\pi} (-1)^{k+j} \cos(\lambda_k(x + b)) \cos(\lambda_j(x' + b)) db \\ & = \frac{(-1)^{k+j}}{(\lambda_j - \lambda_k)(\lambda_j + \lambda_k)} \left(2 \sin(\pi \lambda_j) \cos(\pi \lambda_k) (\lambda_k \sin(\lambda_j x') \sin(\lambda_k x) + \lambda_j \cos(\lambda_j x') \cos(\lambda_k x)) \right. \\ & \quad \left. - 2 \cos(\pi \lambda_j) \sin(\pi \lambda_k) (\lambda_j \sin(\lambda_j x') \sin(\lambda_k x) + \lambda_k \cos(\lambda_j x') \cos(\lambda_k x)) \right) \\ & = 0, \quad (54) \end{aligned}$$

which cancels out as $\sin(\pi \lambda_k)$ and $\sin(\pi \lambda_j)$ will be zero for every j and every k . Moreover, we have:

$$\begin{aligned} & \int_{-\pi}^{\pi} \sin(\lambda_k(x + b)) \sin(\lambda_j(x' + b)) db \\ & = \frac{1}{(\lambda_j - \lambda_k)(\lambda_j + \lambda_k)} \left(2 \sin(\pi \lambda_j) \cos(\pi \lambda_k) (\lambda_j \sin(\lambda_j x') \sin(\lambda_k x) + \lambda_k \cos(\lambda_j x') \cos(\lambda_k x)) \right. \\ & \quad \left. - 2 \cos(\pi \lambda_j) \sin(\pi \lambda_k) (\lambda_k \sin(\lambda_j x') \sin(\lambda_k x) + \lambda_j \cos(\lambda_j x') \cos(\lambda_k x)) \right) \\ & = 0, \quad (55) \end{aligned}$$

which again cancels out for the same reason. Finally, we have:

$$\begin{aligned}
& \int_{-\pi}^{\pi} (-1)^j \sin(\lambda_k(x+b)) \cos(\lambda_j(x'+b)) db \\
&= \frac{(-1)^j}{(\lambda_j - \lambda_k)(\lambda_j + \lambda_k)} \left(2(\cos(\pi\lambda_j) \sin(\pi\lambda_k)(\lambda_j \sin(\lambda_j x') \cos(\lambda_k x) - \lambda_k \cos(\lambda_j x') \sin(\lambda_k x)) \right. \\
&\quad \left. + \sin(\pi\lambda_j) \cos(\pi\lambda_k)(\lambda_j \cos(\lambda_j x') \sin(\lambda_k x) - \lambda_k \sin(\lambda_j x') \cos(\lambda_k x)) \right) \\
&= 0, \tag{56}
\end{aligned}$$

and the same can be shown for $\int_{-\pi}^{\pi} (-1)^k \sin(\lambda_j(x'+b)) \cos(k(x+b)) db$.

Therefore, our derivations simplify to containing only terms where $k = j$:

$$\begin{aligned}
\kappa(x, x') = \int p(w) \int p(b) \left[\lim_{n \rightarrow \infty} \sum_{k=0}^{n-1} (-1)^{2k} \lambda_k^{-4} \left((-1)^k \cos(\lambda_k(wx+b)) + \sin(\lambda_k(wx+b)) \right) \right. \\
\left. \left((-1)^k \cos(\lambda_k(wx'+b)) + \sin(\lambda_k(wx'+b)) \right) \right] dw db. \tag{57}
\end{aligned}$$

Here we can again use the dominated convergence theorem to take the limit outside of the integrals:

$$\begin{aligned}
\kappa(x, x') = \lim_{n \rightarrow \infty} \int p(w) \sum_{k=0}^{n-1} (-1)^{2k} \lambda_k^{-4} \int p(b) \left[\left((-1)^k \cos(\lambda_k(wx+b)) + \sin(\lambda_k(wx+b)) \right) \right. \\
\left. \left((-1)^k \cos(\lambda_k(wx'+b)) + \sin(\lambda_k(wx'+b)) \right) \right] dw db. \tag{58}
\end{aligned}$$

We can now start by calculating the inner integral:

$$\begin{aligned}
& \int p(b) \left[\left((-1)^k \cos(\lambda_k(wx+b)) + \sin(\lambda_k(wx+b)) \right) \right. \\
&\quad \left. \left((-1)^k \cos(\lambda_k(wx'+b)) + \sin(\lambda_k(wx'+b)) \right) \right] db \\
&= \int p(b) \left[\cos(\lambda_k(wx+b)) \cos(\lambda_k(wx'+b)) + \sin(\lambda_k(wx+b)) \sin(\lambda_k(wx'+b)) \right. \\
&\quad \left. + (-1)^k \cos(\lambda_k(wx+b)) \sin(\lambda_k(wx'+b)) \right. \\
&\quad \left. + (-1)^k \cos(\lambda_k(wx'+b)) \sin(\lambda_k(wx+b)) \right] db \\
&= \int p(b) \left[\cos(\lambda_k(wx+b) - \lambda_k(wx'+b)) + (-1)^k \sin(\lambda_k(wx+b) + \lambda_k(wx'+b)) \right] db \\
&= \int p(b) \cos(\lambda_k w(x - x')) db + (-1)^k \underbrace{\int p(b) \sin(\lambda_k w(x + x') + 2\lambda_k b) db}_{=0} \\
&= \cos(\lambda_k w(x - x')) \tag{59}
\end{aligned}$$

Inserting this result into the original equation results in:

$$\kappa(x, x') = \lim_{n \rightarrow \infty} \int p(w) \sum_{k=0}^{n-1} \lambda_k^{-4} \cos(w\lambda_k(x - x')) dw, \tag{60}$$

where we recognise that this the exact same equation encountered in App. A.3 and the terms in the series decrease rapidly towards zero, thus, allowing us to approximate the covariance using only the

Table 2: Priors on the weights corresponding to the spectral density of kernels in the Matérn family.

KERNEL FUNCTION	PRIOR DISTRIBUTION
Exponential ($\nu = 1/2$)	Cauchy(0, 1)
Matérn- ν	t-dist(2ν)
RBF ($\nu \rightarrow \infty$)	N(0, 1)

first term of the sum which gives us (see App. A.3 for analysis on the approximation error):

$$\kappa(x, x') = \int p(w) \cos(w(x - x')) dw = \int p(w) e^{iw(x-x')} dw. \quad (61)$$

Finally, by letting $r = x - x'$, we find that we again recover the spectral density decomposition of a stationary process given by the Wiener–Khinchin theorem, *i.e.*,

$$\kappa(r) = \int p(w) e^{iwr} dw, \quad (62)$$

which concludes the derivation.

B Derivations of Correspondence to the Matérn family

Relating to Sec. 3.3 in the main paper, we provide the following derivation. The spectral density of the Matérn family (*cf.*, Eq. (2)) for the 1D case is given as:

$$S_{\text{Mat.}}(w) = 2\sqrt{\pi} \frac{\Gamma(\nu + \frac{1}{2})}{\Gamma(\nu)} (2\nu)^\nu (2\nu + w^2)^{-(\nu + \frac{1}{2})}, \quad (63)$$

where ν is a smoothness parameter, and we assume unit magnitude and $\ell = 1$ for simplicity. Note that we intentionally used w instead of ω to highlight the correspondence to the prior on the weights. By assuming the prior $p(w)$ to follow a Student- t distribution *i.e.*,

$$p(w) = \frac{\Gamma(\frac{u+1}{2})}{\sqrt{u\pi}\Gamma(\frac{u}{2})} \left(1 + \frac{w^2}{u}\right)^{-\frac{u+1}{2}}, \quad (64)$$

and setting the degree of freedom $u = 2\nu$, we can recover the spectral density of the Matérn family, *i.e.*,

$$\begin{aligned} p(w) &= \frac{\Gamma(\frac{2\nu+1}{2})}{\sqrt{2\nu\pi}\Gamma(\frac{2\nu}{2})} \left(1 + \frac{w^2}{2\nu}\right)^{-\frac{2\nu+1}{2}} &= \frac{\Gamma(\nu + \frac{1}{2})}{\sqrt{2\nu\pi}\Gamma(\nu)} \left(\frac{1}{2\nu}(2\nu + w^2)\right)^{-(\nu + \frac{1}{2})} \\ &= \frac{\Gamma(\nu + \frac{1}{2})}{\sqrt{2\nu\pi}\Gamma(\nu)} (2\nu)^{\nu + \frac{1}{2}} (2\nu + w^2)^{-(\nu + \frac{1}{2})} &= \frac{\Gamma(\nu + \frac{1}{2})}{\sqrt{\pi}\Gamma(\nu)} (2\nu)^\nu (2\nu + w^2)^{-(\nu + \frac{1}{2})} \\ &= \frac{1}{2\pi} 2\sqrt{\pi} \frac{\Gamma(\nu + \frac{1}{2})}{\Gamma(\nu)} (2\nu)^\nu (2\nu + w^2)^{-(\nu + \frac{1}{2})} &= \frac{1}{2\pi} S_{\text{Mat.}}(w). \end{aligned} \quad (65)$$

A summary of the priors on the network weights corresponding to the spectral density of kernels in the Matérn family is given in Table 2.

C Additional Insights

Fourier features, the sinusoidal (or other periodic) basis, and the special dual relationship between stationary covariance functions and the associated spectral density, have been common building blocks in machine learning and signal processing methods for decades. We review connections to Random Fourier features and Fourier methods in GP models.

C.1 Connection to Random Fourier Features

Random Fourier features [43] are a popular technique for randomized, low-dimensional approximations of kernel functions. They are motivated by the observation that the spectral density of a RBF covariance function of a Gaussian process prior can be estimated using Monte Carlo integration. Let $\omega \sim \mathcal{N}(0, 1)$ be Gaussian distributed and $\zeta_\omega(\mathbf{x}) = \exp(i\omega^\top \mathbf{x})$, then

$$\mathbb{E}_\omega[\zeta_\omega(\mathbf{x}), \zeta_\omega(\mathbf{x}')^*] = \int p(\omega) \exp(i\omega^\top \mathbf{r}) d\omega, \quad (66)$$

where $*$ denotes the complex conjugate, is an estimator of the covariance function.

Assuming that ω and \mathbf{x} are real-valued, let b be a value drawn uniformly from $[-\pi, \pi]$, and by replacing the complex exponentials with cosines $z_\omega(\mathbf{x}) = \sqrt{2} \cos(\omega^\top \mathbf{x} + b)$ we obtain:

$$\begin{aligned} \mathbb{E}_\omega[z_\omega(\mathbf{x})z_\omega(\mathbf{x}')] &= \mathbb{E}_\omega[\cos(\omega^\top(\mathbf{x} - \mathbf{x}'))] \\ &= \mathbb{E}_\omega[\mathbb{E}_b[\sqrt{2} \cos(\omega^\top \mathbf{x} + b) \sqrt{2} \cos(\omega^\top \mathbf{x}' + b) \mid \omega]] \quad (\text{Euler's formula}) \\ &\approx \frac{1}{K} \sum_{j=1}^K \sqrt{2} \cos(\omega_j^\top \mathbf{x} + b_j) \sqrt{2} \cos(\omega_j^\top \mathbf{x}' + b_j). \end{aligned} \quad (67)$$

We recognise that the estimate used in random Fourier features is similar to the covariance function of a finite-width single hidden layer network with sinusoidal activation function.

Rahimi and Recht [43] additionally proposed a representation using a composition of a sin and a cosine function, which motivated the use of the sine–cosine activation function in this paper. Sutherland and Schneider [51] later showed that this representation reduces the variance of the estimates when used to approximate the RBF kernel.

C.2 Fourier Methods in Gaussian Process Models

The Fourier duality for stationary covariance functions has been extensively leveraged in Gaussian process models. For gridded inputs, this duality directly allows for leveraging FFT methods to speed up inference and learning. In particular, the sparse spectrum GP (SSGP) method [24] uses the spectral representation of the covariance function to draw random samples from the spectrum. These samples are used to represent the GP on a trigonometric basis, *i.e.*,

$$\phi(\mathbf{x}) = (\cos(2\pi \mathbf{s}_1^\top \mathbf{x}) \sin(2\pi \mathbf{s}_1^\top \mathbf{x}) \dots \cos(2\pi \mathbf{s}_h^\top \mathbf{x}) \sin(2\pi \mathbf{s}_h^\top \mathbf{x})), \quad (68)$$

where the spectral points $\mathbf{s}_r, r = 1, 2, \dots, h$ ($2h = m$) are sampled from the spectral density of the stationary covariance function (following the normalization convention used in the original paper). The covariance function corresponding to the SSGP can be given in the form (*cf.*, Mercer's theorem):

$$\kappa(\mathbf{x}, \mathbf{x}') \approx \frac{2}{m} \phi(\mathbf{x}) \phi^\top(\mathbf{x}') = \frac{1}{h} \sum_{r=1}^h \cos(2\pi \mathbf{s}_r^\top (\mathbf{x} - \mathbf{x}')). \quad (69)$$

This representation of the sparse spectrum method converges to the full GP in the limit of the number of spectral points going to infinity, and is the preferred formulation of the method in one or two dimensions (discussed in [24]). We can interpret the SSGP method in Eq. (69) as a Monte Carlo approximation of the Wiener–Khinchin integral. This interpretation also gives rise to alternative methods for GPs: the methods by Hensman et al. [19] and Solin and Särkkä [48] can be interpreted as a dense/structural (quadrature) approximation to the same integral.

However, for high-dimensional inputs, the SSGP method requires optimization of the frequencies rather than relying on sampling, which is problematic (as discussed in [24]), resulting in a tendency to overfit, and loses the interpretation of the original GP prior in the model. Note that these issues have been addressed in subsequent work. As in SSGPs, our method can be seen as a sampling/optimization approach to a rank-reduced approximation of the induced prior covariance structure. However, the connection we derived retains the role of the prior throughout and generalizes the interpretation of the role of the periodic basis.

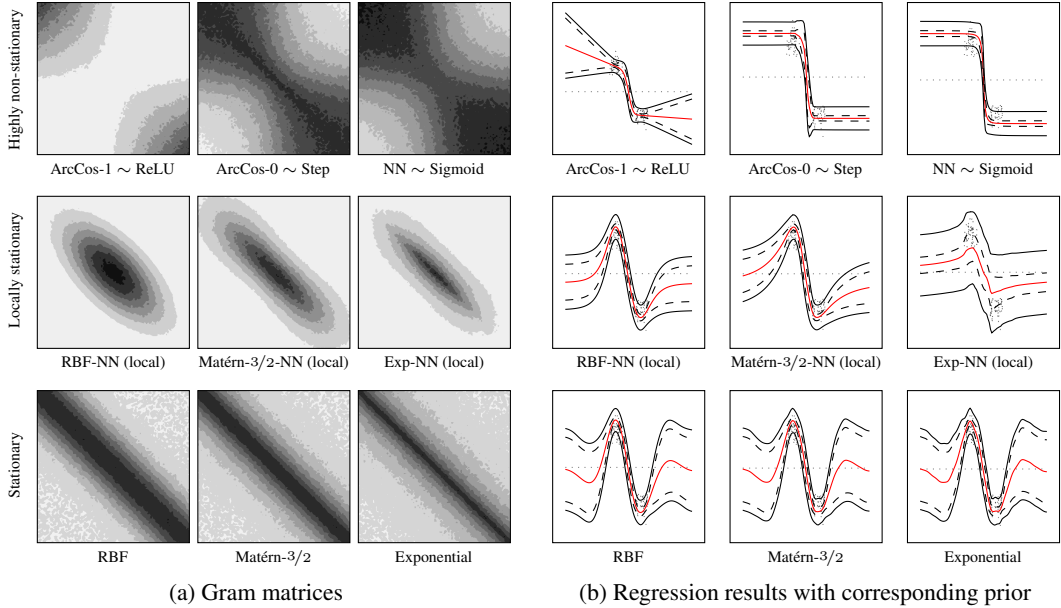


Figure 8: **Left:** Gram matrices (evaluated for $\hat{\kappa}(x, x')$ with 1000 Monte Carlo samples) corresponding to the prior covariance induced by different finite-width NNs (10 hidden units). **Right:** 1D regression results corresponding to the model induced by the prior in the left-hand panels, showing the posterior and predictive 95% intervals of a BNN with ten hidden units obtained through sampling with dynamic HMC for 5000 iterations.

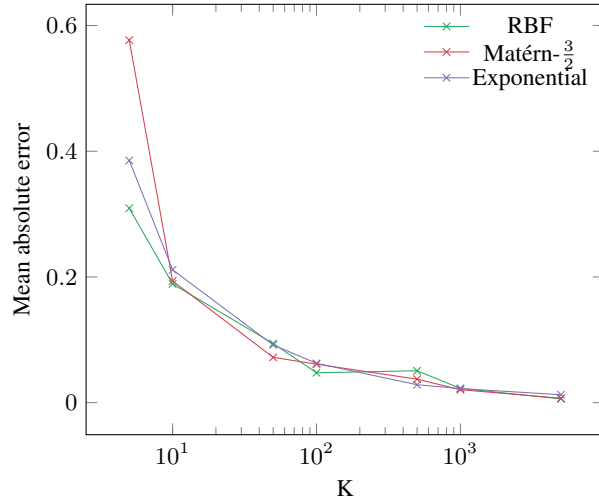


Figure 9: Simulation estimates of the error between the Gram matrix of the limiting process and the Gram matrix of a finite width model with sinusoidal activation functions under increasing number of hidden units (K).

D Experiment Details and Additional Results

Our main contribution is linking globally stationary GP priors to a corresponding infinite-width NN with one hidden layer by specifying activation functions and priors on weights and biases. Most applications, however, require NNs with a deeper structure. In the experiments, this is achieved by considering the preceding NN structure as a feature extractor. The layer containing the model specification is added as the last hidden fully connected layer after the feature extractor part. This means that the activation function and priors for weights and biases only apply to the last hidden layer of the full NN architecture. It is important to note here that we do not mean the final output

layer that produces the class weights or regression output when we refer to the last hidden layer, but the linear layer preceding the output layer. For NN architectures that would not otherwise have a fully connected hidden layer before the output layer, one such layer is added. We refer to this last hidden layer that contains the model implementation as the ‘model layer’. The weights and biases in the model layer are initialized from the prior distributions defined by the model. Table 2 lists prior distributions corresponding to different globally stationary priors. Prior distributions for locally stationary and non-stationary ReLU models are $N(0, 1)$ following the results from [34]. Many of these priors require using periodic activation functions instead of the ReLU, which could be expected to affect trainability. In our experiments, we observed that sometimes training neural networks with periodic activation functions can be a bit harder compared to ReLU networks, but usually, slightly adjusting the learning rate is enough to solve these issues. We expect that the issues with trainability were minor as the periodic activation functions are only used in a single layer of the NN, while other parts of the NN are still using ReLU.

Although our theoretical result considers an infinitely wide NN, we observed in practice that a good result can be obtained if the number of hidden units is sufficiently larger than the dimensionality of the preceding feature space. To avoid using an excessively large number of hidden units, we have added a bottleneck layer for NN architectures for which the feature space after the feature-extraction part would have high dimensionality. This way, we could use a model layer with roughly 100 times more hidden units than the number of dimensions in the preceding feature space.

In the derivations for the prior on the weights, we expected $\ell = 1$ for simplicity. It may be necessary for the model to have a different lengthscale depending on the data in practice. We implemented this by multiplying the weights by a lengthscale parameter before multiplying the input by these weights in the forward pass. This way, we do not need to adjust the prior distribution for the weights as the weights themselves will still stay in the space corresponding to $\ell = 1$. The lengthscale parameter is added as a trainable parameter with a prior of $\ell \sim \Gamma(\alpha = 2, \beta = 0.5)$, which is weakly informative.

The model layer produces hidden features which are mapped to outputs using the linear output layer. The weights for the output layer are initialized from $N(0, 1/\kappa)$. The output $f(x)$ dimensionality equals the number of classes in classification tasks and one in regression tasks. Based on this output, the data likelihood needs to be calculated for the loss function. For regression tasks the data likelihood is $N(y - f(x) | 0, s^2)$, where s is the standard deviation of the measurement noise which we include into the model as a trainable parameter with prior $\Gamma(\alpha = 0.5, \beta = 1)$. For classification, the data likelihood is calculated by applying the softmax function on $f(x)$ to map the outputs to probabilities and then choosing the class probability corresponding to the class y .

To train the model, we construct a loss function that considers both the data likelihood and the prior distributions. Since our goal is to fit an approximate posterior distribution on the model parameters, we use the Bayes formula to obtain a loss function that is directly proportional to the posterior distribution:

$$p(w, b, \ell, s | y, x) \propto p(y | x) p(w) p(b) p(\ell) p(s). \quad (70)$$

For optimization purposes we take a negative logarithm of the product of priors and data likelihood, which also changes this to a minimization problem, resulting in the following loss function:

$$\mathcal{L} = -\log p(y | x) - \log p(w) - \log p(b) - \log p(\ell) - \log p(s). \quad (71)$$

Here $p(y | x)$ is the data likelihood described above (for classification the cross entropy loss directly gives $-\log p(y|x)$ from the outputs $f(x)$), $p(w)$ is the prior on weights, $p(b)$ is the prior on biases, $p(\ell)$ is the prior on lengthscale, and $p(s)$ is the prior on measurement noise variance (for classification $-\log p(s) = 0$). For NN architectures that have a feature-extractor part preceding the model layer, we also include standard L2-regularization on the parameters of the feature-extractor network to prevent the model from completely bypassing the defined priors by learning extreme values for feature-extractor network parameters. For globally stationary models $p(b) = \text{Uniform}(-\pi, \pi)$, meaning that the bias term is defined on a constrained space. We therefore optimise $\hat{b} \in \mathbb{R}$, which is defined on an unconstrained space, and apply the map/link function $b = 2\pi \text{sigmoid}(\hat{b}) - \pi$.

The calculations for obtaining the experiment results were mostly performed using computer resources within the Aalto Science-IT project. These resources included both CPU nodes and GPU nodes (NVIDIA V100 and Tesla P100). Some results were also calculated on local GPU resources (NVIDIA RTX 2080). All of the utilized data sets are publicly available and widely used, and none of them contain any personally identifiable information or offensive content. The illustrative toy BNN

examples are implemented using HMC in Turing.jl [14], GP regression results use GPflow [33], and all other experiments are implemented using PyTorch [41].

D.1 Illustrative Toy Examples

The NN model architecture for the illustrative toy examples contains only the model layer with 30 hidden units and the output layer. The posterior estimates are obtained through dynamic HMC sampling [14] run for 10k iterations and four independent chains. Fig. 1 shows predictive densities for non-stationary, locally stationary, and globally stationary activation functions on the banana classification task. The top row illustrates the predictive densities of infinite-width BNNs (GP), and the bottom row shows corresponding results for a finite-width BNN. We observe that models with global stationarity-inducing activation functions revert to the prior outside the data, leading to conservative behaviour (high uncertainty) for out-of-domain samples. Moreover, we see that the finite-width BNNs result in similar behaviour to their infinite-width counterpart, while the locally stationary activation functions in finite-width BNNs exhibit a slower reversion to the mean than their infinite-width corresponding GPs. Fig. 10 shows additional BNN results for the same experiment for globally stationary models using different periodic activation functions. We see that we obtain similar results regardless of the choice of the periodic activation function. As expected, all periodic activation functions result in low variance only for the training data clusters and revert to the prior outside the data. Fig. 11 shows the effect of varying the number of hidden units in the same experiment.

Additionally, we include a 1D toy regression study highlighting the differences between different prior assumptions encoded by choice of the activation function. Fig. 2 shows the corresponding prior covariance as well as posterior predictions for the infinite-width (GP) model. In Fig. 8, we replicate the same study with a finite-width network and recover the same behaviour. For the finite-width results, posterior estimates are obtained through dynamic HMC sampling for 5000 iterations. Fig. 9 illustrates the error between the Gram matrices of the infinite width and finite width models.

D.2 Benchmark Regression Tasks

For the UCI [8] regression tasks, the NN architecture is a fully connected network with layers d -1000-1000-500-25-2000-1. A dropout layer with $p = 0.1$ is applied at the 500 nodes wide layer to prevent overfitting. For these experiments, we used a 10-fold cross-validation setup performed for a single repetition per experiment. Each model is trained for 100 epochs using SGD (momentum 0.9). The batch sizes used for each data set are listed in Table 3. The learning rates for the lengthscale parameter ℓ and measurement noise standard deviation s were set to 0.01. All learning rates were decreased to 0.72 of the original value during training, using a schedule having square root dependence on the progression through epochs (slower than linear learning rate decay). The lengthscale parameter ℓ was initialized with a value of five, and s was initialized with one. For the non-stationary ReLU model, the lengthscale parameter does not have a similar significance as in the global and local stationary models and therefore was initialized with a value of one to prevent vanishing or exploding gradients. Posterior inference was performed using KFAC Laplace [45].

Since we observed that the results were sensitive to the SGD learning rate and the variance scale parameter of KFAC Laplace, we performed a grid search over both of these hyperparameters. Therefore, we split the training set such that 80% is used for training and the remaining 20% is used as a validation set for the grid search. First, a grid search for the SGD learning rate was performed over the values $[5 \times 10^{-5}, 1 \times 10^{-4}, 5 \times 10^{-4}, 1 \times 10^{-3}]$, choosing the learning rate that achieved the smallest RMSE on the validation set. A single common learning rate was chosen for all ten folds. Subsequently, KFAC Laplace was applied on models trained using the best learning rate, using variance scales in the grid $[0.01, 0.05, 0.1, 0.15, 0.2, 0.25]$. 30 samples were used for model averaging in the grid search. As the objective in the KFAC Laplace variance scale grid search, we used a weighted sum of validation set data negative log-likelihood and an OOD noise validation set negative log-likelihood [22]. We used $\lambda = 0.2$ as the parameter controlling the weighting between the regular validation set score and the OOD noise set score (one-fifth of the weight on the OOD set). A single common KFAC Laplace variance scale was chosen for all ten folds. After the best learning rate and KFAC Laplace variance scale has been selected, the model is retrained from the start on the full training set of each fold using the best learning rate. KFAC Laplace model with the best variance scale is then fitted on the trained model, and 50 samples from the approximate posterior are used for model averaging to obtain the final results.

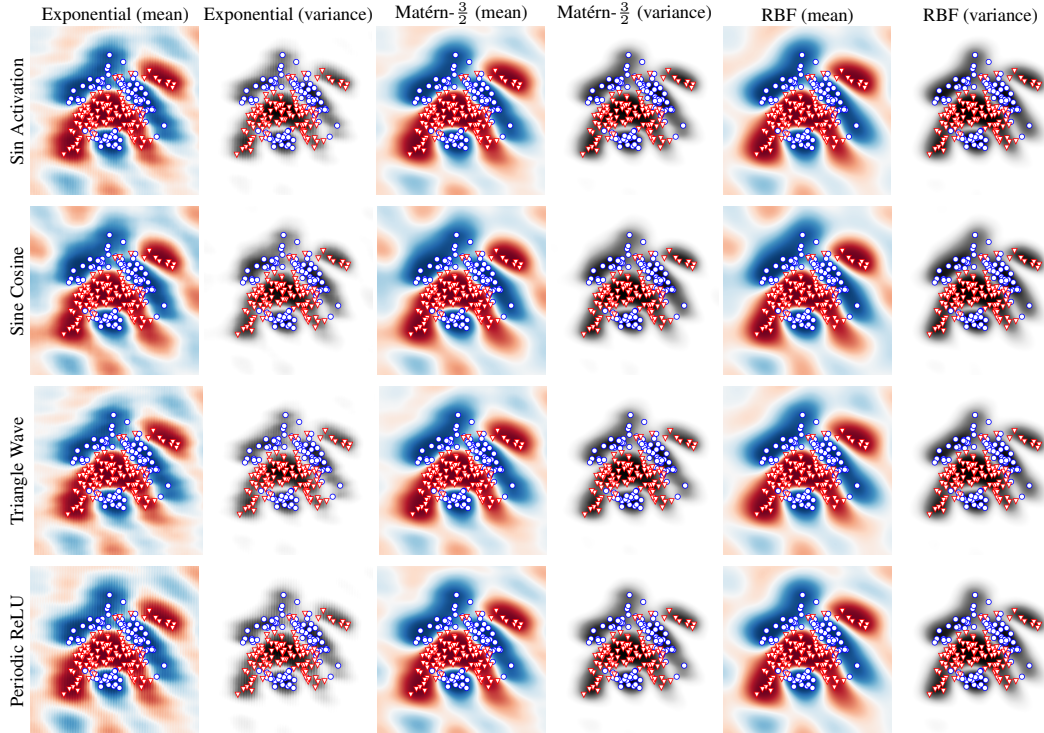


Figure 10: Posterior predictive densities of globally stationary BNNs with 30 hidden units on the banana classification task. Table rows show results for different periodic activation functions, and columns show different prior covariance functions. For each model, the resulting predictive mean and variance are plotted side by side. For predictive mean plots, the colour intensity represents confidence in the class prediction. For the variance plots, white colour represents high variance, and black colour represents low variance. We obtain comparable results regardless of the choice of the periodic activation function. Estimated using dynamic HMC run for 10k iterations and 4 chains.

The results for the boston (2–3 h), concrete (2–3 h) and airfoil (6–8 h) data sets were calculated using a single CPU per experiment, and the results for the elevators (1–2 h) data set were calculated using a single GPU per experiment. Copyright of the concrete data set: Prof. I-Cheng Yeh [62].

Table 3 shows results on four UCI regression data sets comparing deep neural networks with ReLU, locally stationary RBF [60], and locally stationary Matérn- $3/2$ and Matérn- $5/2$ [34] against global stationary models. Table 3 lists root mean square error (RMSE) and negative log predictive density (NLPD), which captures the predictive uncertainty, while the RMSE only accounts for the mean. The table lists mean and standard deviation values across folds of the 10-fold cross-validation. The values for the best performing models are shown in bold. Especially on small data sets, the standard deviation values are large, which is mostly due to differences between different folds instead of variations in model performance. The table shows that global stationary models provide better estimates of the target distribution in all cases while obtaining comparable RMSEs. Moreover, we observe that the periodic ReLU activation function tends to outperform the sinusoidal activation. Also, the importance of the choice of prior covariance can be seen in Table 3. It appears that the Matérn- $3/2$ covariance is the best choice for the smallest boston data set, while the smoother Matérn- $5/2$ or RBF covariance functions seem to be more suitable for the larger data sets.

D.3 Benchmark Classification Tasks

The experimental setup for the UCI [8] classification tasks is the same as for the regression tasks, apart from the following details. For the UCI classification tasks, the NN architecture is a fully connected network with layers d -1000-1000-500-25-2000- c . The batch sizes used for each data set are listed in Table 4. The lengthscale parameter ℓ was initialized at value one.

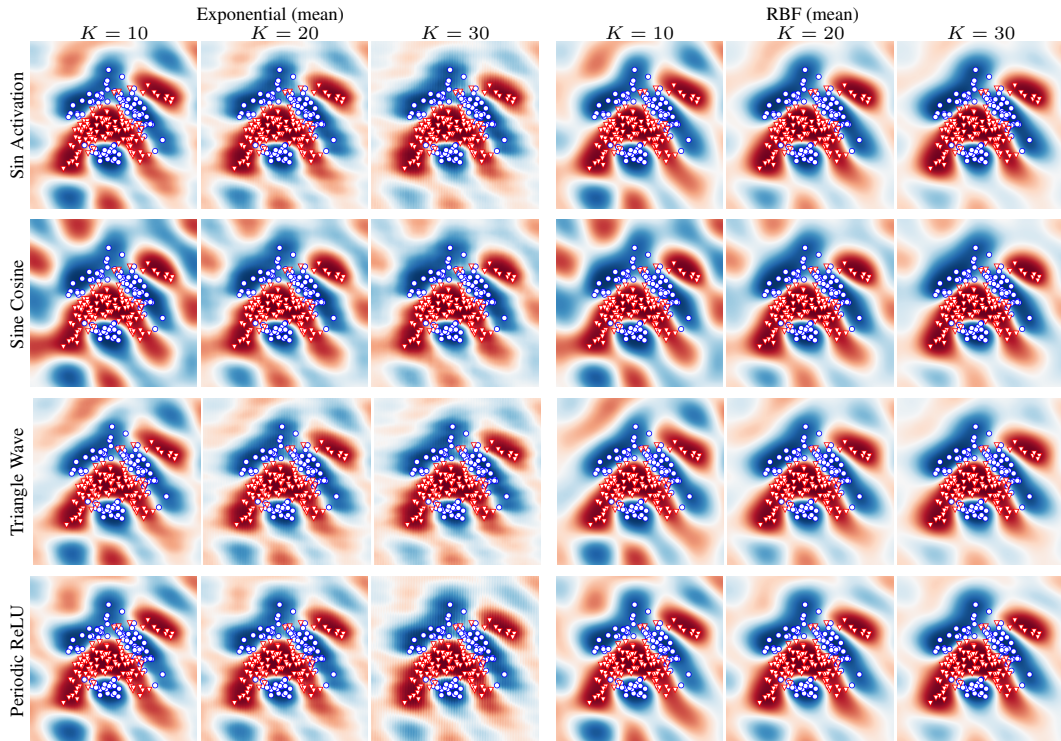


Figure 11: Posterior predictive densities of stationary BNNs for varying number of hidden units K on the banana classification task. Table rows show results for different periodic activation functions, and columns show different number of hidden units, denoted as K . Results are shown for the two extreme cases, *i.e.* Exponential and RBF kernel. We obtain comparable results for all periodic activation function. Results are estimated using dynamic HMC run for 10k iterations and 4 chains.

Table 3: Examples of UCI regression tasks, showing the globally stationary NN model directly gives competitive mean negative log predictive density (NLPD) and root mean square error (RMSE) to locally stationary and non-stationary NN models. KFAC Laplace was used as the inference method.

(n, d) (c, n_{batch})	BOSTON (506, 12) (1, 50)		CONCRETE (1030, 5) (1, 50)		AIRFOIL (1503, 5) (1, 50)		ELEVATORS (16599, 18) (1, 500)	
	NLPD	RMSE	NLPD	RMSE	NLPD	RMSE	NLPD	RMSE
ReLU	0.51±0.32	0.37±0.07	0.78±0.16	0.48±0.04	0.51±0.53	0.41±0.21	0.38±0.03	0.35±0.01
loc RBF	0.52±0.30	0.37±0.08	0.78±0.22	0.44±0.05	0.10±0.15	0.26±0.03	0.41±0.04	0.35±0.01
glob RBF (sin)	0.42±0.34	0.36±0.07	0.74±0.15	0.49±0.05	0.14±0.17	0.29±0.05	0.38±0.03	0.35±0.01
glob RBF (tri)	0.44±0.38	0.36±0.09	0.75±0.16	0.49±0.05	0.08±0.11	0.27±0.03	0.38±0.03	0.35±0.01
loc Mat-5/2	0.74±0.42	0.36±0.07	0.87±0.19	0.47±0.04	0.14±0.16	0.27±0.03	0.41±0.04	0.35±0.01
glob Mat-5/2 (sin)	0.41±0.33	0.36±0.08	0.67±0.09	0.47±0.03	0.05±0.12	0.26±0.03	0.37±0.04	0.35±0.01
glob Mat-5/2 (tri)	0.45±0.38	0.36±0.09	0.65±0.09	0.46±0.03	0.05±0.16	0.26±0.03	0.37±0.03	0.34±0.01
loc Mat-3/2	0.71±0.38	0.40±0.08	0.84±0.28	0.42±0.04	0.11±0.18	0.26±0.03	0.43±0.04	0.35±0.01
glob Mat-3/2 (sin)	0.43±0.27	0.39±0.08	0.73±0.16	0.49±0.05	0.07±0.15	0.27±0.03	0.37±0.03	0.35±0.01
glob Mat-3/2 (tri)	0.46±0.39	0.36±0.09	0.71±0.14	0.48±0.04	0.19±0.43	0.34±0.21	0.37±0.03	0.35±0.01
glob RBF (sincos)	0.50±0.36	0.37±0.08	0.73±0.13	0.49±0.04	0.19±0.21	0.30±0.07	0.38±0.02	0.35±0.01
glob Mat-5/2 (sincos)	0.41±0.23	0.39±0.08	0.72±0.12	0.49±0.04	0.04±0.11	0.26±0.03	0.38±0.03	0.35±0.01
glob Mat-3/2 (sincos)	0.35±0.32	0.34±0.07	0.68±0.14	0.47±0.04	0.05±0.16	0.27±0.04	0.56±0.54	0.42±0.21
glob RBF (prelu)	0.39±0.30	0.36±0.07	0.74±0.14	0.49±0.04	0.05±0.12	0.26±0.03	0.74±0.73	0.46±0.21
glob Mat-5/2 (prelu)	0.50±0.42	0.37±0.08	0.64±0.11	0.46±0.04	0.08±0.16	0.27±0.04	0.37±0.03	0.35±0.01
glob Mat-3/2 (prelu)	0.38±0.22	0.38±0.08	0.72±0.18	0.48±0.05	0.08±0.12	0.27±0.03	0.39±0.03	0.36±0.01

The results for the diabetes (3–4 h) data set were calculated using a single CPU per experiment, and the results for the adult (4–6 h), connect-4 (6–8 h) and covtype (8–12 h) data sets were calculated

Table 4: Examples of UCI classification tasks, showing the globally stationary NN model directly gives competitive accuracy and mean negative log predictive density (NLPD) to non-stationary and locally stationary NN models. KFAC Laplace was used as the inference method.

(n, d) (c, n_{batch})	DIABETES (768, 8) (2, 50)		ADULT (45222, 14) (2, 500)		CONNECT-4 (67556, 42) (3, 500)		COVTYPE (581912, 54) (7, 500)	
	NLPD	ACC	NLPD	ACC	NLPD	ACC	NLPD	ACC
ReLU	0.48±0.05	0.76±0.04	0.31±0.01	0.85±0.00	0.57±0.01	0.82±0.00	0.18±0.00	0.93±0.00
loc RBF	0.48±0.04	0.76±0.04	0.31±0.01	0.85±0.00	0.54±0.01	0.81±0.00	0.19±0.01	0.93±0.00
glob RBF (sin)	0.48±0.05	0.77±0.04	0.32±0.01	0.85±0.00	0.61±0.02	0.81±0.00	0.18±0.01	0.93±0.00
glob RBF (tri)	0.48±0.05	0.77±0.04	0.31±0.01	0.85±0.00	0.61±0.01	0.82±0.00	0.18±0.01	0.93±0.00
loc Mat-5/2	0.52±0.04	0.78±0.06	0.32±0.01	0.85±0.00	0.50±0.01	0.81±0.00	0.22±0.00	0.92±0.00
glob Mat-5/2 (sin)	0.48±0.04	0.77±0.04	0.31±0.01	0.85±0.00	0.64±0.03	0.82±0.00	0.17±0.01	0.93±0.00
glob Mat-5/2 (tri)	0.48±0.04	0.77±0.04	0.31±0.01	0.85±0.00	0.64±0.03	0.82±0.00	0.17±0.00	0.93±0.00
loc Mat-3/2	0.49±0.04	0.76±0.05	0.32±0.01	0.85±0.01	0.53±0.01	0.81±0.00	0.19±0.01	0.93±0.00
glob Mat-3/2 (sin)	0.48±0.04	0.77±0.04	0.32±0.01	0.85±0.00	0.66±0.03	0.81±0.00	0.17±0.01	0.93±0.00
glob Mat-3/2 (tri)	0.48±0.04	0.78±0.04	0.32±0.01	0.85±0.00	0.66±0.02	0.81±0.00	0.18±0.01	0.93±0.00
glob RBF (sincos)	0.48±0.05	0.77±0.05	0.32±0.01	0.85±0.00	0.61±0.01	0.82±0.00	0.18±0.00	0.93±0.00
glob Mat-5/2 (sincos)	0.48±0.04	0.76±0.04	0.31±0.01	0.85±0.00	0.64±0.02	0.82±0.00	0.17±0.01	0.93±0.00
glob Mat-3/2 (sincos)	0.48±0.04	0.76±0.04	0.32±0.01	0.85±0.00	0.66±0.03	0.81±0.01	0.18±0.00	0.93±0.00
glob RBF (prelu)	0.48±0.05	0.77±0.04	0.31±0.01	0.85±0.00	0.61±0.02	0.82±0.00	0.18±0.00	0.93±0.00
glob Mat-5/2 (prelu)	0.47±0.04	0.77±0.04	0.32±0.01	0.85±0.00	0.64±0.02	0.81±0.00	0.18±0.00	0.93±0.00
glob Mat-3/2 (prelu)	0.48±0.04	0.77±0.05	0.32±0.01	0.85±0.00	0.65±0.02	0.81±0.00	0.18±0.01	0.93±0.00

Table 5: Examples of UCI classification tasks, showing the globally stationary NN model directly gives competitive area under receiver operating characteristic curve (AUC) to non-stationary and locally stationary NN models. KFAC Laplace was used as the inference method.

(n, d) (c, n_{batch})	DIABETES (768, 8) (2, 50)		ADULT (45222, 14) (2, 500)		CONNECT-4 (67556, 42) (3, 500)		COVTYPE (581912, 54) (7, 500)	
	AUC	AUC	AUC	AUC	AUC	AUC	AUC	
ReLU	0.84±0.03	0.91±0.00	0.91±0.00	0.90±0.00	0.90±0.00	0.99±0.00	0.99±0.00	
loc RBF	0.84±0.03	0.91±0.00	0.91±0.00	0.90±0.00	0.90±0.00	0.99±0.00	0.99±0.00	
glob RBF (sin)	0.84±0.03	0.91±0.00	0.91±0.00	0.90±0.00	0.90±0.00	0.99±0.00	0.99±0.00	
glob RBF (tri)	0.84±0.03	0.91±0.00	0.91±0.00	0.90±0.00	0.90±0.00	0.99±0.00	0.99±0.00	
loc Mat-5/2	0.84±0.03	0.91±0.00	0.91±0.00	0.89±0.00	0.89±0.00	0.99±0.00	0.99±0.00	
glob Mat-5/2 (sin)	0.84±0.03	0.91±0.00	0.91±0.00	0.90±0.00	0.90±0.00	0.99±0.00	0.99±0.00	
glob Mat-5/2 (tri)	0.83±0.03	0.91±0.00	0.91±0.00	0.90±0.00	0.90±0.00	0.99±0.00	0.99±0.00	
loc Mat-3/2	0.84±0.03	0.91±0.00	0.91±0.00	0.90±0.00	0.90±0.00	0.99±0.00	0.99±0.00	
glob Mat-3/2 (sin)	0.84±0.03	0.91±0.00	0.91±0.00	0.90±0.00	0.90±0.00	0.99±0.00	0.99±0.00	
glob Mat-3/2 (tri)	0.84±0.03	0.91±0.00	0.91±0.00	0.90±0.01	0.90±0.01	0.99±0.00	0.99±0.00	
glob RBF (sincos)	0.83±0.04	0.91±0.00	0.91±0.00	0.90±0.00	0.90±0.00	0.99±0.00	0.99±0.00	
glob Mat-5/2 (sincos)	0.83±0.03	0.91±0.00	0.91±0.00	0.90±0.00	0.90±0.00	0.99±0.00	0.99±0.00	
glob Mat-3/2 (sincos)	0.84±0.03	0.91±0.00	0.91±0.00	0.90±0.01	0.90±0.01	0.99±0.00	0.99±0.00	
glob RBF (prelu)	0.84±0.03	0.91±0.00	0.91±0.00	0.90±0.00	0.90±0.00	0.99±0.00	0.99±0.00	
glob Mat-5/2 (prelu)	0.84±0.03	0.91±0.00	0.91±0.00	0.90±0.00	0.90±0.00	0.99±0.00	0.99±0.00	
glob Mat-3/2 (prelu)	0.84±0.03	0.91±0.00	0.91±0.00	0.90±0.01	0.90±0.01	0.99±0.00	0.99±0.00	

using a single GPU per experiment. Copyright of the covtype data set: Jock A. Blackard and Colorado State University.

Table 4 and Table 5 show results on standard UCI [8] classification data sets comparing results for different activation functions. We compare a neural network with a non-stationary model using the ReLU activation function to both local stationary [34] and global stationary models for different covariance functions. Table 4 lists predictive accuracies and negative log predictive densities (NLPD) for each model. Moreover, Table 5 lists the area under the receiver operating characteristic curve (AUC) for the different models. The tables lists mean and standard deviation values across folds of the 10-fold cross-validation. The values for the best performing models are shown in bold. The classification results indicate that there are very few differences in the performance between the different models and that global stationary models achieve competitive predictive accuracy, NLPD, and AUC compared to the locally stationary and non-stationary models.

For the UCI classification tasks, we performed additional experiments using SWAG [29], inference instead of KFAC Laplace. The experiment setup here was also 10-fold cross-validation. The NN architecture is a fully connected network with layer widths d -1000-1000-500-50- c for all models. The models were trained for 20 epochs using batch sizes listed in Table 6 with Adam optimizer and a learning rate of 1×10^{-4} . The learning rate for the lengthscale parameter ℓ was separately set to 0.01 and initialized with one. A schedule was used for the Adam learning rates, decreasing them to one-tenth of the current value at epochs 10 and 15. The SWAG model was collected for 40 epochs (with $M = 20$ samples to estimate the covariance matrix) using SGD (momentum 0.9) as

Table 6: Examples of UCI classification tasks, showing the globally stationary NN model directly gives competitive accuracy and mean negative log predictive density (NLPD) to non-stationary and locally stationary NN models. SWAG was used as the inference method.

(n, d) (c, n_{batch})	DIABETES (768, 8) (2, 50)		ADULT (45222, 14) (2, 500)		CONNECT-4 (67556, 42) (3, 500)		COVTYPE (581912, 54) (7, 500)	
	NLPD	ACC	NLPD	ACC	NLPD	ACC	NLPD	ACC
ReLU	0.53±0.07	0.75±0.03	0.38±0.15	0.79±0.18	0.54±0.12	0.79±0.04	0.19±0.00	0.92±0.00
loc RBF	0.49±0.05	0.76±0.04	0.33±0.01	0.85±0.00	0.47±0.01	0.81±0.00	0.19±0.00	0.93±0.00
glob RBF (sin)	0.51±0.05	0.76±0.04	0.35±0.03	0.85±0.00	0.51±0.05	0.81±0.01	0.18±0.00	0.93±0.00
glob RBF (tri)	0.53±0.07	0.73±0.04	0.33±0.01	0.85±0.00	0.51±0.05	0.81±0.01	0.19±0.01	0.92±0.00
loc Mat-5/2	0.49±0.05	0.76±0.04	0.32±0.01	0.85±0.00	0.47±0.01	0.82±0.00	0.25±0.01	0.91±0.00
glob Mat-5/2 (sin)	0.53±0.07	0.74±0.04	0.34±0.02	0.85±0.01	0.49±0.01	0.81±0.00	0.18±0.00	0.93±0.00
glob Mat-5/2 (tri)	0.52±0.05	0.73±0.03	0.34±0.01	0.85±0.00	0.50±0.03	0.81±0.01	0.19±0.00	0.92±0.00
loc Mat-3/2	0.49±0.04	0.75±0.03	0.32±0.01	0.85±0.00	0.47±0.01	0.82±0.00	0.23±0.01	0.91±0.00
glob Mat-3/2 (sin)	0.57±0.07	0.73±0.04	0.35±0.02	0.84±0.00	0.50±0.01	0.81±0.00	0.19±0.01	0.92±0.00
glob Mat-3/2 (tri)	0.55±0.07	0.74±0.04	0.34±0.01	0.85±0.01	0.50±0.02	0.80±0.00	0.19±0.00	0.93±0.00
glob RBF (sincos)	—	—	0.37±0.10	0.83±0.07	0.54±0.07	0.80±0.01	0.18±0.01	0.93±0.00
glob Mat-5/2 (sincos)	—	—	0.34±0.02	0.85±0.01	0.52±0.03	0.81±0.01	0.18±0.01	0.93±0.00
glob Mat-3/2 (sincos)	0.58±0.05	0.72±0.03	0.39±0.11	0.81±0.08	0.51±0.02	0.81±0.00	0.18±0.01	0.93±0.00
glob RBF (prelu)	0.52±0.06	0.76±0.04	0.34±0.01	0.85±0.00	0.50±0.01	0.81±0.00	0.19±0.01	0.92±0.00
glob Mat-5/2 (prelu)	0.53±0.05	0.75±0.03	0.33±0.01	0.85±0.00	0.49±0.01	0.81±0.00	0.19±0.00	0.92±0.00
glob Mat-3/2 (prelu)	0.58±0.07	0.73±0.03	0.34±0.01	0.85±0.00	0.49±0.01	0.81±0.00	0.19±0.01	0.93±0.00

Table 7: Examples of UCI classification tasks, showing the globally stationary NN model directly gives competitive area under receiver operating characteristic curve (AUC) to non-stationary and locally stationary NN models. SWAG was used as the inference method.

(n, d) (c, n_{batch})	DIABETES (768, 8) (2, 50)		ADULT (45222, 14) (2, 500)		CONNECT-4 (67556, 42) (3, 500)		COVTYPE (581912, 54) (7, 500)	
	AUC	AUC	AUC	AUC	AUC	AUC	AUC	AUC
ReLU	0.82±0.04	0.82±0.04	0.87±0.12	0.87±0.12	0.86±0.08	0.86±0.08	0.99±0.00	0.99±0.00
loc RBF	0.83±0.03	0.83±0.03	0.91±0.00	0.91±0.00	0.90±0.00	0.90±0.00	0.99±0.00	0.99±0.00
glob RBF (sin)	0.82±0.04	0.82±0.04	0.90±0.01	0.90±0.01	0.89±0.01	0.89±0.01	0.99±0.00	0.99±0.00
glob RBF (tri)	0.81±0.04	0.81±0.04	0.91±0.00	0.91±0.00	0.89±0.01	0.89±0.01	0.99±0.00	0.99±0.00
loc Mat-5/2	0.84±0.03	0.84±0.03	0.91±0.00	0.91±0.00	0.90±0.00	0.90±0.00	0.99±0.00	0.99±0.00
glob Mat-5/2 (sin)	0.80±0.05	0.80±0.05	0.90±0.01	0.90±0.01	0.89±0.01	0.89±0.01	0.99±0.00	0.99±0.00
glob Mat-5/2 (tri)	0.81±0.04	0.81±0.04	0.90±0.00	0.90±0.00	0.89±0.01	0.89±0.01	0.99±0.00	0.99±0.00
loc Mat-3/2	0.83±0.03	0.83±0.03	0.91±0.00	0.91±0.00	0.90±0.01	0.90±0.01	0.99±0.00	0.99±0.00
glob Mat-3/2 (sin)	0.79±0.04	0.79±0.04	0.90±0.01	0.90±0.01	0.89±0.00	0.89±0.00	0.99±0.00	0.99±0.00
glob Mat-3/2 (tri)	0.81±0.04	0.81±0.04	0.90±0.01	0.90±0.01	0.89±0.01	0.89±0.01	0.99±0.00	0.99±0.00
glob RBF (sincos)	—	—	0.85±0.16	0.85±0.16	0.88±0.02	0.88±0.02	0.99±0.00	0.99±0.00
glob Mat-5/2 (sincos)	—	—	0.90±0.00	0.90±0.00	0.88±0.01	0.88±0.01	0.99±0.00	0.99±0.00
glob Mat-3/2 (sincos)	0.78±0.03	0.78±0.03	0.84±0.15	0.84±0.15	0.88±0.01	0.88±0.01	0.99±0.00	0.99±0.00
glob RBF (prelu)	0.81±0.04	0.81±0.04	0.91±0.01	0.91±0.01	0.89±0.00	0.89±0.00	0.99±0.00	0.99±0.00
glob Mat-5/2 (prelu)	0.81±0.03	0.81±0.03	0.90±0.01	0.90±0.01	0.89±0.01	0.89±0.01	0.99±0.00	0.99±0.00
glob Mat-3/2 (prelu)	0.79±0.03	0.79±0.03	0.91±0.01	0.91±0.01	0.89±0.01	0.89±0.01	0.99±0.00	0.99±0.00

the optimizer, updating the posterior estimate once per epoch. The lengthscale parameter is kept fixed during the SWAG model collection, as no SWAG posterior estimate is collected for it. The learning rate for SGD in the SWAG model collection part (the SWAG learning rate) was selected using Bayesian optimization with BoTorch in the range $(1 \times 10^{-4}, 3)$, selecting the value providing the best negative log-likelihood on the validation set. We used one-fifth of the training set of the current fold for validation, and after selecting the best SWAG learning rate we trained the model from the beginning using the full training set for each fold using the best performing SWAG learning rate. We used a fixed value for ℓ equal to what the earlier optimization ended at (this is to prevent ending up in a different local optimum where the optimized SWAG learning rate does not provide good results). Each models SWAG learning rate was optimized individually, but a common SWAG learning rate was used for all ten folds of a single experiment. For model averaging, 50 samples from the approximate posterior were sampled. The SWAG results for all UCI classification data sets were calculated on a single GPU per experiment and the rough running times for each data set were diabetes: 2–4 h, adult 6–8 h, connect-4 8–10 h and covtype 15–20 h. For the SWAG results, Table 6 lists predictive accuracies and NLPDs, and Table 7 lists AUC values for the different models. The results show that similar to the KFAC Laplace results, the global stationary models using periodic activation functions achieve competitive predictive accuracy, NLPD, and AUC compared to the locally stationary and non-stationary models. The main difference to results obtained using KFAC Laplace is that SWAG seems to produce more variability in the results between different models. The missing values in Table 6 and Table 7 are due to the optimization diverging in the SWAG model collection phase.

D.4 Detection of Distribution Shift with Rotated MNIST

For the MNIST ([25], available under CC BY-SA 3.0) digit classification experiment, the feature extractor part of the NN architecture has two convolutional layers (32 and 64 channels, both using a 3×3 kernel) followed by a fully connected layer taking the dimensionality down to 25, and the following model layer has 2000 hidden units. The models were trained on the MNIST training set for 50 epochs using a batch size of 64 with an SGD optimizer (learning rate 1×10^{-3} , momentum 0.9), using only unrotated images. A schedule was used for the SGD learning rates, decreasing them to 0.9 of the current value at epochs 25 and 37. The learning rate for the lengthscale parameter ℓ was set to 1×10^{-4} , and was initialized with 0.2. The posterior inference was performed using KFAC Laplace [45] with a fixed variance scale of one. For model averaging, we used 30 posterior samples. We tested the trained model on the standard unrotated MNIST test set and rotated versions of the same test set for rotation angles every 10° up to 360° . Running this experiment for one model on one GPU took roughly 2 hours due to testing the model on multiple test sets.

Fig. 5 shows the results on the rotated MNIST experiment for different models. We evaluate the predictive accuracy, mean confidence of the predicted class, and NLPD on the rotated test sets. The results indicate that all models obtain similar accuracy results, while only local and global stationary models do not result in over-confident uncertainty estimates. For an ideally calibrated model, the mean confidence would decrease as low as the accuracy curve when the digits are rotated, which would keep the NLPD values as low as possible. We see that even for the local and global stationary models, the mean confidence has a minimum of around 0.55 while the accuracy decreases below 0.2. We also observe that the NLPD curves rise to high values (over 3) for the better performing models. The accuracy of all models increases near the 180° rotation. This is most likely due to numbers 0, 1 and 8 appearing similar with 0° and 180° rotations. Interestingly, the NLPD values for the local and global stationary models hardly decrease for the rotation angle of 180° although the accuracy for this angle increases compared to adjacent angles. This could be due to number 6 looking like number 9 at 180° rotation, and vice versa, causing the model to make overconfident incorrect predictions. Although, this kind of overconfident misclassification cannot be prevented even with a correctly calibrated model, as samples of one class genuinely appear to belong to another class.

Fig. 12 shows additional results on the rotated MNIST experiment for different models, using only a maximum a posteriori (MAP) estimate for the model parameters. The models used for the MAP results are the same trained models that were used for the results in Fig. 5, but for the MAP results the KFAC Laplace inference step is skipped. The MAP results are almost identical to the KFAC Laplace results, except that 90° and 270° rotations for mean confidence have slightly higher values for the MAP results. This suggests that the KFAC Laplace inference might not be very successful in improving data set shift detection properties in this experiment.

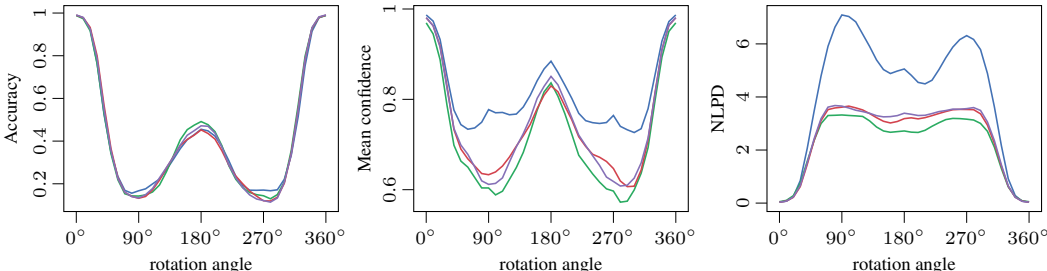


Figure 12: Rotated MNIST maximum a posteriori (MAP) results: The models have been trained on unrotated digits. The test-set digits are rotated at test time to show the sensitivity of the trained model to perturbations. Model predictions are based on a MAP estimate of model parameters. All models perform equally in terms of accuracy, while ReLU (—) shows overconfidence in terms of mean confidence and NLPD. The stationary RBF models (— local, — sin, — sin-cos) capture uncertainty.

D.5 Out-of-distribution Detection Using CIFAR-10, CIFAR-100, and SVHN

For this experiment, the feature extractor part is a GoogLeNet [52] followed by a 512 node wide model layer. Pre-trained weights are used for the feature extractor part of the NN, and kept unchanged during the model training (pre-trained model from https://github.com/huyvnphan/PyTorch_CIFAR10). The models were trained on CIFAR-10 [23] for 20 epochs using a batch size of 128 with Adam optimiser and a learning rate of 1×10^{-4} . The learning rate for the lengthscale parameter ℓ was separately set to 1×10^{-5} , and the lengthscale parameter was initialised with one. The posterior inference was performed using SWAG [29]. The SWAG model was collected for 40 epochs ($M = 20$) using SGD (momentum 0.9) as the optimiser, updating the posterior estimate once per epoch. The lengthscale parameter is kept fixed during the SWAG model collection. The learning rate for SGD in the SWAG model collection part (the SWAG learning rate) was selected using Bayesian optimisation with BoTorch in the range $(1 \times 10^{-4}, 3)$ based on the negative log-likelihood on the validation set. As validation data, we used the CIFAR-10 test set. Using the CIFAR-10 test set as the validation set for selecting hyperparameters is valid here; as for this experiment, the focus is not on measuring the performance on the test set but evaluating OOD detection performance on the CIFAR-100 and SVHN test sets. After selecting the best SWAG learning rate, we trained the model from the beginning using the best performing SWAG learning rate and a fixed value for ℓ equal to the earlier optimisation. For each model, the SWAG learning rate was optimised individually. For model averaging, 30 samples from the approximate posterior of the parameters were sampled to calculate the predictions on CIFAR-10, CIFAR-100 [23], and SVHN [39]. Running this experiment for one model on one GPU took roughly one day due to the Bayesian optimization process.

Fig. 14 compares model performance on out-of-distribution detection for image classification for non-stationary, local stationary and global stationary models. Both CIFAR-100 (more similar) and SVHN (more dissimilar to CIFAR-10) images are OOD data, and the models should show high uncertainties (high predictive entropy, high predictive variance) for the respective test images. The histograms of predictive entropies for different test sets show that most models can separate between in-distribution and OOD data based on this metric. However, the predictive marginal variance histograms show that the global stationary models can better detect the OOD samples compared to ReLU and local stationary models. Interestingly, the ReLU model shows higher variance on CIFAR-100 images compared to SVHN images, although SVHN images are more different from the training set images. For global stationary models, both entropy and variance histograms show that the models clearly consider SVHN more OOD than CIFAR-100, which is intuitive as CIFAR-100 resembles CIFAR-10 more than SVHN. Fig. 14 also shows sample images for most/least similar to the training data distribution that the model has learned. Looking at these images for different models, we can see that for CIFAR-10, images with dark background result in high uncertainty for all models. For the CIFAR-100 sample images, the global stationary Matérn- $3/2$ model has classified pictures of animals and humans with the highest confidence, which seems intuitive as these could be considered resembling some of the CIFAR-10 classes (for example, dogs or cats). Moreover, the images with the highest uncertainty seem visually very different from CIFAR-10 images. For the SVHN sample images, all models seem to be most confident about clear and sharp images and blurry images result in high uncertainty, which is reasonable as CIFAR-10 images usually have clear shapes. However, this is again most apparent for the global stationary models, suggesting the model has learned meaningful representations of the input space.

Using the same results that are visualized in the histograms in Fig. 14, we calculated area under receiver operating characteristic curve (AUC) and area under precision-recall curve (AUPR) values for OOD detection in the CIFAR-10 experiment to provide additional quantitative results, treating either CIFAR-100 or SVHN as the OOD data set. We calculated the AUC and AUPR measures using the marginal variance as the metric to determine whether a sample is OOD or not. We consider this a better metric for OOD detection compared to predictive entropy, as in-distribution samples that are hard to classify are expected to have high predictive entropy, not necessarily allowing the detection of OOD samples based on this metric. Table 8 lists the calculated AUC and AUPR numbers. The results for SVHN as the OOD data set indicate a clear difference between the non-stationary (ReLU) and the stationary (local and global) models. The globally stationary RBF model achieves the best AUC score. Treating CIFAR-100 as an OOD set is not as straightforward considering numerical AUC and AUPR comparisons. CIFAR-100 images are visually very similar to CIFAR-10 images but representing different classes, and hence can be considered not strictly OOD. For example, it is reasonable to expect that even a correctly operating model may consider some CIFAR-100 images

Table 8: Table of numerical results on the image classification OOD task. The results used to calculate the numbers in this table are the same that were used to create histograms in Fig. 14. The table lists the area under receiver operating characteristic curve (AUC) and the area under precision-recall curve (AUPR) for each of the models. Numbers are calculated both for considering CIFAR-100 or SVHN as the OOD set, while CIFAR-10 is the in-distribution data. The table also visualizes whether each model considers CIFAR-100 or SVHN more OOD based on which data set is detected as OOD more effectively.

OOD data set	AUC		AUPR	
	CIFAR-100	SVHN	CIFAR-100	SVHN
ReLU	0.974	>	0.961	0.970
loc RBF	0.976	<	0.987	0.976
glob RBF (sin)	0.942	<	0.988	0.995
loc Mat-3/2	0.973	<	0.983	0.993
glob Mat-3/2 (sin)	0.965	<	0.981	0.993

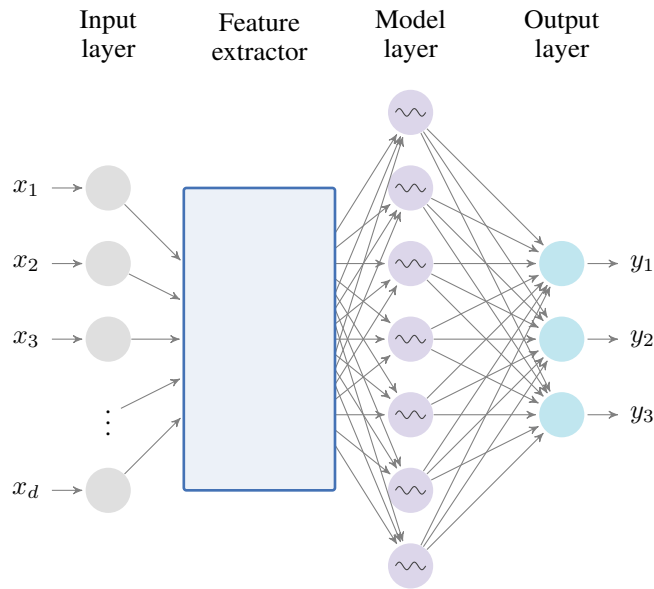
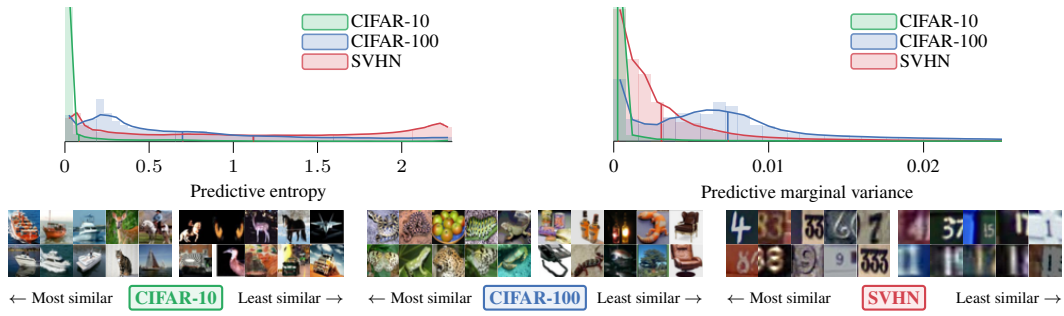


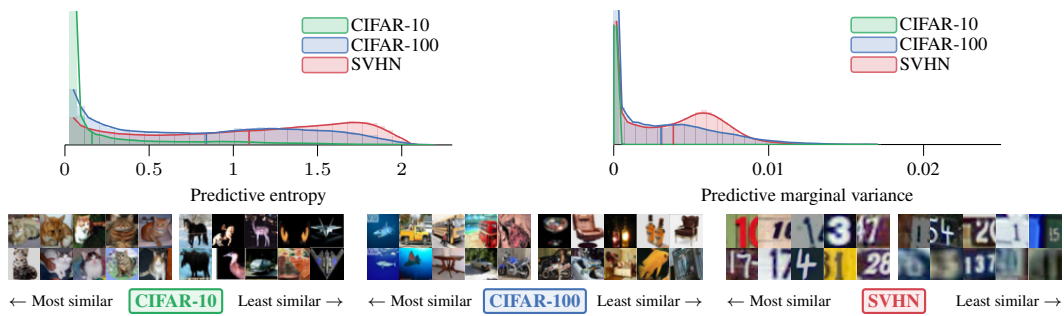
Figure 13: An illustrative figure describing the model architecture. The model first passes an input $\mathbf{x} \in \mathbb{R}^d$ into a feature extractor. The feature extractor part is a task dependent neural network architecture, which can be for example a fully connected structure or some convolutional layers. The feature extractor results in some L -dimensional representation (in the illustration $L = 3$), which is followed by a fully connected hidden layer (referred to as model layer in the text) resulting in a K dimensional representation ($K = 7$ in the figure). The model specific activation function is applied on this K -dimensional representation (sinusoidal activation in the figure). The output $\mathbf{y} \in \mathbb{R}^c$ is produced by a fully connected output layer. Here c is the number of classes in case of a classification task ($c = 3$ in the figure).

more in-distribution than the most difficult or visually peculiar CIFAR-10 test images. For this reason, it is reasonable to compare AUPR and AUC numbers of each model for the two OOD data sets, CIFAR-100 and SVHN, and observe which data set is considered more OOD. We expect SVHN to be considered more OOD, which is true except for the ReLU model based on the AUC metric.

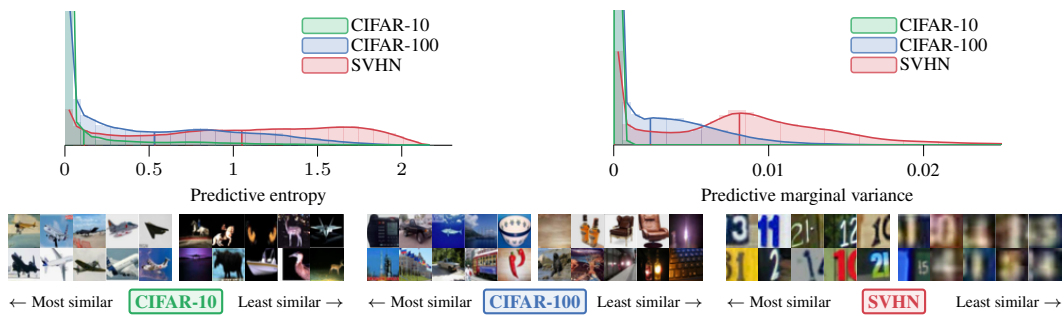
Results with ReLU model



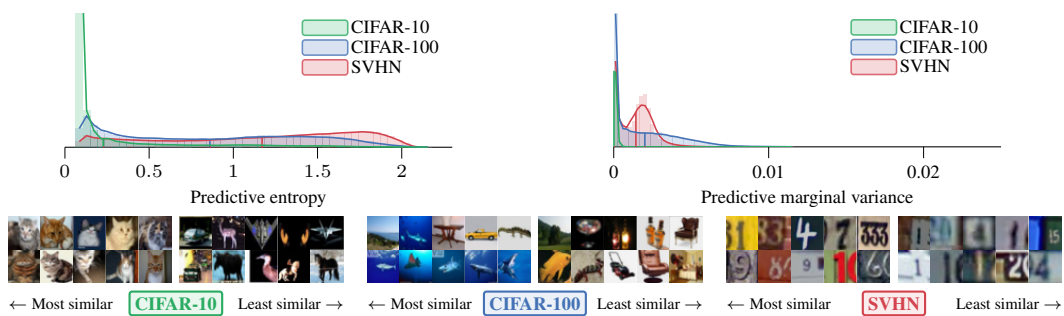
Results with locally stationary RBF model



Results with globally stationary RBF model (sinusoidal)



Results with locally stationary Matérn- $\frac{3}{2}$ model



Results with globally stationary Matérn- $\frac{3}{2}$ model (sinusoidal)

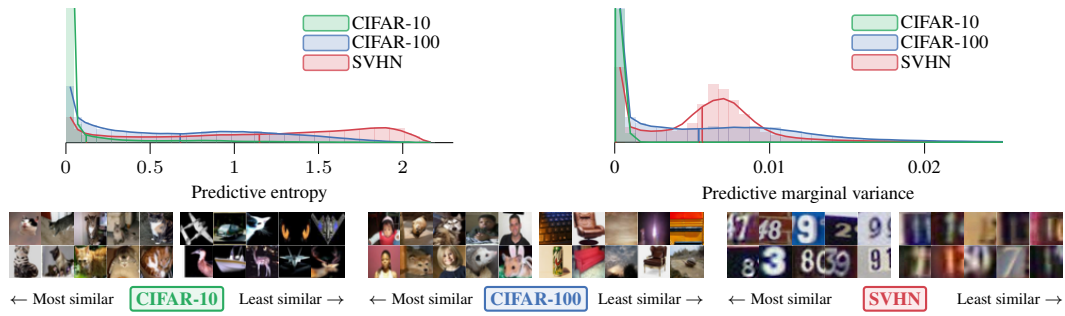


Figure 14: OOD detection experiment results for models trained on CIFAR-10 and tested on CIFAR-10, CIFAR-100, and SVHN. Predictive entropy histograms of test image results are on the left, and predictive marginal variance histograms are on the right. On the bottom are sample images from each test set: left-side images with lowest entropy/highest confidence, and right-side images with highest entropy/lowest confidence.